

1 **Multi-tier mechanics control stromal adaptations in swelling lymph nodes**

2

3 Frank P. Assen^{1,2,*}, Miroslav Hons^{1,3}, Robert Hauschild¹, Shayan Shamipour¹, Jun Abe⁴, Walter A.
4 Kaufmann¹, Tommaso Costanzo¹, Gabriel Krens¹, Markus Brown¹, Burkhard Ludwig⁵, Simon
5 Hippenmeyer¹, Jens V. Stein⁴, Carl-Philipp Heisenberg¹, Edouard Hannezo¹, Sanjiv A. Luther⁶, Michael
6 Sixt^{1,*}

7

8 ¹Institute of Science and Technology Austria (IST Austria), Klosterneuburg, Austria

9 ²Department of Dermatology, Medical University Vienna, Vienna, Austria

10 ³BIOCEV, First Faculty of Medicine, Charles University, Vestec, Czech Republic

11 ⁴Department of Oncology, Microbiology and Immunology, University of Fribourg, Fribourg,

12 Switzerland

13 ⁵Institute of Immunobiology, Kantonsspital St Gallen, St Gallen, Switzerland

14 ⁶Department of Biochemistry, University of Lausanne, Epalinges, Switzerland

15

16 *Correspondence to: Sixt@ist.ac.at; frank.assen@meduniwien.ac.at

17

18 **Abstract**

19 Lymph nodes (LNs) comprise two main structural elements: Fibroblastic reticular cells (FRCs)
20 that form dedicated niches for immune cell interaction and capsular fibroblasts that build a
21 shell around the organ. While LNs are fairly stable in size during homeostatic conditions,
22 immunological challenge causes more than 10-fold increase in size within only a few days.
23 How a solid organ can accommodate such extreme volumetric changes is poorly
24 understood. Here, we characterize the biomechanics of LN swelling on the cellular and
25 organ scale. We identify lymphocyte trapping by influx and proliferation as drivers of an
26 outward pressure force, causing FRCs and their associated conduits to stretch. After an
27 initial phase of relaxation, FRCs sense the resulting strain via cell matrix adhesions, which
28 coordinates local growth and remodeling of the stromal network. While the expanded FRC
29 network adopts its typical configuration, a massive fibrotic reaction of the organ capsule
30 sets in and counters further organ expansion. Thus, different fibroblast populations
31 mechanically control LN swelling in a multi-tier fashion.

32 **Introduction**

33 Lymph nodes (LNs) are the macroscopic organs of the adaptive immune system. As opposed
34 to other organs, the LN parenchyma only contains few resident cells, while the bulk of
35 lymphocytes is in transit. Lymphocytes circulate through the bodies' vascular systems, and
36 from there they enter LNs via high endothelial venules (HEVs). Within the LN parenchyma,
37 lymphocytes actively migrate to scan large numbers of potentially antigen-bearing dendritic
38 cells (DCs). After several hours of unsuccessful search, lymphocytes exit the organ again via
39 efferent lymphatic vessels that eventually drain back into the blood circulation and the cycle
40 starts again^{1,2}. Lymphocytes are densely packed within LNs and make up about 95% of its
41 total cellularity. Despite dynamic cellular exchange, homeostatic LN size remains relatively
42 stable. Known modulators of homeostatic LN cellularity (e.g., during circadian rhythms^{3,4})
43 are mainly chemoattractants and adhesion molecules^{2,5-8}, which serve as entry and exit
44 signals for lymphocytes, as well as stromal cell-derived survival factors⁹⁻¹² and adrenergic
45 signals^{13,14}. The main stromal cells found in LNs are FRCs. These form the non-hematopoietic
46 backbone of the organ and deposit bundled fibers of extracellular matrix (ECM) that
47 assemble an intricate 3D network termed conduits. FRCs enwrap these ECM conduits and
48 form an interface with the immune cells^{15,16}. They provide a multitude of signals that serve
49 to compartmentalize the organ and support migration, cellular interactions and expansion
50 of immune cell subsets¹⁷⁻¹⁹.

51 Upon immunological challenge, reactive LNs swell rapidly by recruiting large numbers of
52 naïve lymphocytes via HEVs, while lymphocyte egress via efferent lymphatics is initially
53 blocked^{20,21}. LNs can swell up to 10-fold in size in the order of days, imposing an internal
54 structural problem on the FRC network that has to cope with this volumetric challenge. It
55 has been demonstrated that FRCs are able to relax and expand upon interaction with
56 activated DCs^{22,23}. This has been proposed as one mechanism that allows the LN to create
57 additional space during the swelling phase. In addition, FRC numbers expand during
58 inflammation and various redundant mechanisms that drive this expansion in the early and
59 late phase of LN swelling have been described^{20,22-26}. The ratio of FRC- to lymphocyte
60 numbers remains fairly constant in the swelling LN and trapping of naïve lymphocytes in the
61 absence of inflammatory stimuli has been demonstrated as a sufficient stimulus for the FRC
62 network to expand²⁰. How network expansion is coordinated to prevent under- or

63 overgrowth of the FRC network is unknown, and although mechanical forces are obvious
64 feedback parameters, these aspects of LN swelling have not been measured until to date.
65 We measure the cellular and mechanical changes accompanying LN swelling and show that
66 mechanical load on the conduit network and subsequent FRC mechanosensing are central
67 to expansion of the FRC network and LN growth.
68

69 Results

70 The reactive lymph node resists swelling

71 To understand the global mechanical behavior of LNs while expanding, we started out with
72 a quantitative characterization of bulk tissue properties of the reactive organ. Upon
73 immunization with keyhole limpet hemocyanin in complete Freund's adjuvant (KLH/CFA) in
74 footpads of wild-type (wt) mice, we observed a more than 10-fold increase in volume of
75 draining popliteal LNs after 14 days, when the organ reached its maximum size. The volume
76 was calculated from 2D side-view images, which correlated well with the weight of the
77 organ and showed that LNs swell on average about 0.75 mm^3 per day (Figure 1A,B & Figure
78 S1A,B). We measured tissue mechanics by compressing explanted popliteal LNs between
79 two parallel plates at 75% of their original height (25% strain), while the resisting force
80 exerted by the LN on the top plate was measured over a time period of 20-60 minutes
81 (Figure 1C). During this time the LN underwent a viscoelastic relaxation behavior and
82 reached a new force-equilibrium, which is described by the stress-relaxation curve (Figure
83 1D & Figure S1C,D). Together with the geometrical parameters of LNs measured before
84 compression and at the new force-equilibrium, the *effective resistance* (σ , *surface tension*),
85 the *viscosity* (μ_2 , fluidic resistance to deformation by an applied force), and the *elastic*
86 *modulus* (Young's Modulus, or elastic resistance to deformation by an applied force) of the
87 tissue were derived by modelling the parameters to a generalized Kelvin model (Figure
88 S1E)²⁷. At equilibrium (long time scale), the LN resisted the external force exerted by the
89 plate, which sets the *effective resistance* (given in Newton/m). This parameter describes the
90 collective forces resisting organ expansion and is a measure of how much force is necessary
91 to drive the swelling of the LN by a certain length scale.

92 During the course of organ expansion (D0-D14), we observed a ~4-fold increase of effective
93 resistance and values remained elevated until the endpoint at D14 (Figure 1E). Viscosity –
94 the resistance to deformation on the medium time scale – only increased in the last phase
95 of swelling, while elasticity – the resistance to deformation on the short time scale – was
96 selectively increased from the homeostatic condition at D2 and D14 of inflammation (Figure
97 1F,G).

98 These data demonstrate that tissue properties of LNs show complex adaptive dynamics
99 upon swelling, and suggest that the mechanical features of the organ resist the forces
100 driving expansion.

101

102 **Lymphocyte numbers generate pressure and drive lymph node swelling**

103 Having defined that mechanical properties of the LN resist swelling, we next asked what are
104 the internal forces driving organ expansion. Lymphocytes constantly recirculate through LNs
105 where they are densely packed within the FRC scaffold (Figure S1F). Entry via HEVs,
106 blocking of exit in the early inflammation phase, and proliferation upon activation are the
107 main factors that increase cellularity of the node, making these potential factors driving
108 expansion²⁸⁻³⁰. Hence, we manipulated entry and activation and tested the impact on LN
109 bulk tissue properties.

110 We first perturbed lymphocyte entry under homeostatic conditions using an L-selecting
111 antagonizing antibody; anti-CD62L (α -CD62L). L-selectin is expressed on naïve lymphocytes
112 and rate-limiting for transmigration via HEVs³¹. After 24h of either α -CD62L or PBS
113 intravenous (i.v.) injection, popliteal LNs from wt mice were harvested and used for parallel
114 plate compression experiments. We found that blocking of lymphocyte entry significantly
115 reduced LN volume, effective resistance and viscosity, while the Young's Modulus remained
116 unchanged (Figure 2A-E). These data suggest that lymphocyte influx represents an internal
117 force, balancing the effective resistance of the homeostatic LN.

118 Next, we asked how lymphocyte cellularity affects bulk tissue properties of LNs during
119 inflammatory swelling. In order to distinguish between contribution of recirculating and
120 locally proliferating lymphocytes, we treated wt or OT-II mice with either α -CD62L or PBS,
121 immunized with KLH/CFA and measured tissue properties after four days (Figure 2F-J). Mice
122 carrying the OT-II TCR transgene suppress their natural TCRs³¹, thereby creating a situation
123 where lymphocyte homing is maintained but the majority of B and T cell responses against
124 the mismatched KLH antigen eliminated. Homing, and to a lesser extent proliferation,
125 contributed significantly to LN swelling, while elimination of both parameters reduced LN
126 volumes even further (Figure 2G). In agreement with the findings under homeostatic
127 conditions, α -CD62L administration reduced the effective resistance in both wt and OT-II
128 mice, with blockade of homing showing the dominant effect (Figure 2H). While the viscosity
129 in the tested conditions did not show a clear trend with lymphocyte cellularity, the Young's

130 Modulus was reduced when lymphocyte trafficking was blocked in inflammation (Figure
131 2I,J).

132 Thus, lymphocyte trapping is not a consequence of LN swelling but drives the process as it
133 generates an outward pressure force which is countered by the organ's effective resistance.

134

135 **The FRC network stretches upon lymph node swelling**

136 Next, we investigated which mechanical features of the LN are resisting its expansion. The
137 two candidate structures mediating the LNs effective resistance to swelling are the organ
138 capsule, and the FRC- and conduit network. To understand how the FRC network adapts to
139 volumetric changes upon swelling we quantified FRC spacing (gaps) within the T zone over
140 the time course of inflammation in Ccl19-Cre; mTmG (FRC-mGFP) (membrane Tomato,
141 membrane Green Fluorescent Protein (GFP)) mice that selectively express membrane GFP
142 (mGFP) in FRCs^{32,33}. To this end, a circle-fitting algorithm was used to quantify the
143 distribution of gaps in FRC networks from two-dimensional (2D) tissue sections (Figure
144 3A,B). While we found no obvious disruptions of network integrity, the FRC network
145 dynamically adapted over time. In the first four days of inflammation the FRC network
146 widened, as indicated by larger gaps, and in the following days returned to homeostatic
147 levels (Figure 3C,D).

148 These results suggest that the intact FRC network initially stretches upon swelling and
149 subsequently remodels to accommodate the increased numbers of proliferating and
150 immigrating lymphocytes.

151

152 **Conduits are stretched in the swelling lymph node**

153 The FRC network comprises two principal structural components: the FRC itself and the ECM
154 conduit, a complex fibrillar structure, which the myofibroblastic FRC both produces and
155 ensheathes (Figure 4A). Both components have the potential to bear load and confer
156 mechanical resistance to swelling. In the following, we devised strategies to quantitatively
157 measure if and to what extent the two structures experience mechanical forces. We started
158 out with the ECM component and as a proxy for mechanical strain, we chose to investigate
159 the structural organization of the conduit's fibrillar collagen. Like in tendons and other
160 elastic ECM structures, fibrillar alignment should increase with strain.

161 We fixed homeostatic and reactive LNs and removed all cellular components by alkali-
162 maceration (Figure S2A,B). To resolve the 3-dimensional (3D) organization of individual
163 collagen fibrils, scanning transmission electron microscopy (STEM) tomograms of T zone
164 conduits were acquired at 2 degrees differential tilting angles (Figure 4A). 3D images were
165 reconstructed using computed weight back projection (Figure S2C,D). We quantified the
166 extent of conduit stretching by 3D manual tracking of individual collagen fibril segments and
167 by computationally calculating the centerline of each conduit based on the average
168 direction of its collagen fibrils. This allowed us to determine the angle of misalignment of
169 individual fibril segments relative to the centerline (Figure 4C,D). We found that compared
170 to homeostasis (D0), early in inflammation (D2, D4) conduit collagen fibrils become
171 progressively aligned, whereas later in inflammation (D14) they again adopted a misaligned
172 configuration (Figure 4D).

173 These results suggest that conduits stretch and bear an increased mechanical load early
174 upon LN swelling. At later time points they revert to the homeostatic state. Initial stretching
175 and later adaptation are well in line with our previous findings on network configuration.

176

177 **FRC network tension increases upon lymph node swelling**

178 We next addressed the cellular component of the FRC stretching-response. To study if the
179 previously observed change in conduit conformation is mirrored by the tension-state of the
180 FRC network, we directly measured FRC network tension by intravital laser ablation and
181 recoil analysis^{34,35}. To this end, inguinal LNs of FRC-mGFP mice were surgically exposed and
182 the FRC network was imaged around 20 μm below the capsule. Individual strands of the 3D
183 network were cut using a high-power ultra-violet (UV)-laser (Figure 5A). FRC network
184 tension was subsequently determined in kymographs by calculating local recoil velocities of
185 the region around the site of ablation (Figure 5B,C and Supplemental Movie 1). We found
186 that at D4 and D8 of inflammation the tension on the FRC network almost doubled and was
187 restored again to homeostatic levels at D14 of inflammation.

188 As a proxy for the cellular mechano-response, we next measured the nuclear vs. cytoplasmic
189 intensity of the transcription factors Yes-associated protein (YAP), and transcriptional co-
190 activator with PDZ binding motif (TAZ), which are well-established downstream responses of
191 cytoskeletal tension³⁶. FRCs and endothelial cells stained positive for YAP/TAZ, while no
192 signal could be observed in leukocytes (Figure 5D,E). The nuclear:cytoplasmic ratio of

193 YAP/TAZ (N:C YAP/TAZ ratio) in FRCs remained stable from D0 to D2 of inflammation but
194 increased at D4 and D8 of inflammation, confirming that FRCs experience increased
195 cytoskeletal tension during LN swelling. The N:C ratio decreased after FRC tension peaked
196 (Figure 5C,F), thereby faithfully recapitulating the tension as measured by laser cutting.
197 Interestingly, after two weeks of inflammation we observed a large population of FRCs that
198 had a negative N:C ratio, suggesting that those cells were completely shielded from active
199 tension.

200 Together, these data demonstrate that FRC tension increases upon LN swelling. However,
201 compared with the ECM conduit (Figure 4), tension at the cellular level increases with a two
202 day time delay. This kinetic is well in line with previous observations, suggesting that early in
203 inflammation FRCs experience a relaxation of actomyosin contractility^{22,23}. This relaxation is
204 transient and followed by an increase in cytoskeletal tension. At later time points when
205 network geometry adopts its homeostatic configuration, tension drops again.

206

207 **FRCs in the swelling lymph node undergo distributed clonal expansion**

208 The above data suggest that lymphocyte influx drives LN expansion, which initially stretches
209 the FRC network and elicits a mechanosensitive response by the cells, once their initial
210 relaxation^{22,23} ceases. We next wanted to understand how the FRC network expands,
211 remodels and re-establishes its typical configuration and mechanical state, while
212 maintaining structural integrity.

213 To this end, we devised an approach to map the spatio-temporal expansion of the FRC
214 network in the swelling LN *in situ*. We used a sparse clonal labeling approach named Mosaic
215 Analysis with Double Markers (MADM)³⁷⁻³⁹. MADM labeling depends on rare
216 interchromosomal mitotic recombination driven by Cre-loxP sites (Figure S3A,B). Two
217 reciprocally split GFP and tdTomato genes (GT and TG) on identical loci of homologous
218 chromosomes are used to create transheterozygous offspring (GT/TG). Interchromosomal
219 recombination can take place in G₂ phase and restores functional GFP and tdTomato
220 expression. To trigger rare recombination specifically in FRCs we used the Ccl19-Cre
221 transgene³². When followed by X-segregation of chromosomes in mitosis, two daughter
222 cells are formed in which one expresses GFP (green lineage) and the other tdTomato (red
223 lineage). Recombination is irreversible and all subsequent progeny cells become part of the
224 lineage.

225 Homeostatic and reactive LNs were cleared and imaged by 3D light-sheet fluorescence
226 microscopy (LSFM). In reactive nodes, prominent clusters of FRCs emerged at D4 and D8 of
227 inflammation, while such clusters were rarely observed in homeostasis (Figure 6A,B & Figure
228 S3C). This suggested that individual FRC clones expanded following immunization and that
229 daughter-FRCs stay close to their precursor. No substantial bias in red vs. green lineage was
230 apparent, justifying combined analyses (Figure S3D). FRC clusters were quantitatively
231 analyzed using a density-based spatial clustering of applications with noise (DBSCAN)⁴⁰ for
232 which FRC bodies were semi-automatically mapped in 3D as spheres with a 12 μm diameter
233 (Figure S3E). A cluster was defined as at least three FRCs from the same lineage within a
234 radius of 20 μm . We found that both the number of labeled FRCs, number of clusters and
235 number of FRCs in clusters were significantly increased in reactive nodes (Figure 6C-F). Since
236 clusters can arise by chance, the cluster results were compared to the average of 10
237 simulated distributions in which the same number of FRCs were randomly distributed in the
238 same volume. Although clusters arise by chance in random distributions, FRCs in
239 inflammation were less uniformly distributed and formed more and larger clusters with FRC
240 numbers ranging from 3-14 (Figure 6G, Figure S3F). Clone size distribution was exponential
241 as is expected from an equipotent population of precursors that are dividing
242 stochastically⁴¹. To quantify the extent of FRC clustering within LNs, we defined a cluster
243 factor (CF) as the ratio of the number of FRCs found in clusters between the observed and
244 simulated distributions (Figure S3G). Hence, a CF of 100 indicates that 100x more cells are
245 found in clusters as by chance alone. We found an average CF of 5 in homeostatic conditions
246 and 117 in inflammation (respectively, 70 and 165 for D4 and D8), confirming that FRCs
247 form clusters in the swelling LN (Figure 6H).

248 We next investigated if FRC clusters are found at the vicinity of HEVs in the swelling LN as it
249 has been shown that *de novo* FRCs can derive from perivascular fibroblasts in the
250 developing spleen^{42,43}. To this end, the CF was plotted as a function of the distance from
251 HEVs. No enrichment of clusters was found at these specific perivascular areas (Figure 6I).

252 To better understand the relationships between the measured parameters a correlation-
253 matrix was created (Figure 6J). As expected, the number of labeled FRCs correlated with the
254 number of observed clusters and the number of FRCs found in clusters, while the number of
255 clusters correlated well with the number of FRCs found in clusters. In the reactive LN *de*
256 *novo* MADM-events can occur, but our data indicate that these do not affect the CF as the

257 CF is independent of the number of labeled FRCs, and the relative numbers of FRC in
258 clusters remains unchanged in inflammation (Figure 6J, Figure S3H). LN volume was the best
259 determinant for the CF and also correlated well with the number of labeled FRCs, number of
260 clusters and FRCs in clusters (Figure 6J,K).

261 Together, these data show that FRCs expand in randomly distributed clusters and that FRC
262 growth correlates with LN volume (Figure 6K). This suggests that FRCs can expand in
263 response to local signals independent of their localization.

264

265 **Talin1 is required for FRC mechanosensing.**

266 Given our previous observations, mechanical forces appeared as an attractive feedback
267 parameter regulating FRC network growth. Mechano-coupling of fibroblasts to their
268 underlying matrix is mediated by integrins and their associated intracellular force-sensitive
269 adaptor molecule talin. FRCs express both Talin1 and Talin2 isoforms which play non-
270 redundant roles in integrin activation and force transduction⁴⁴. We selectively deleted
271 Talin1 in FRCs by generating *Ccl19-Cre; Talin1^{fl}* (FRC^{ΔTLN1}) mice.

272 Peripheral LNs of FRC^{ΔTLN1} mice were reduced in size and had lowered levels of the T-zone
273 chemokine CCL21 in the paracortex and the T cell zone was significantly reduced in size in
274 FRC^{ΔTLN1} LNs (FigureS4A-C). Within the T cell zone podoplanin (PDPN)+ FRCs^{ΔTLN1} still formed
275 a regularly interconnected network and expressed intercellular adhesion molecule 1 (ICAM-
276 1) and vascular cell adhesion molecule 1 (VCAM-1), arguing for regular differentiation
277 (Figure S4D). Within HEVs, CCL21 levels were unaffected (Figure S4B). Hence, despite the
278 reduced size, the basic organization and differentiation of the Talin1 deficient FRC network
279 was maintained. When FRC^{ΔTLN1} mice were immunized with KLH, LN swelling was substantial
280 (Figure7A) and during the initial four days after immunization, relative weight gain was
281 comparable to control mice. A mild reduction was only seen at D14. This demonstrates that
282 lymphocyte influx and proliferation were still occurring within the Talin deficient FRC
283 network, emphasizing the suitability of the genetic model to ask the principal question, if
284 FRC mechanosensing is required for network adaptation.

285 When we analyzed N:C YAP/TAZ ratio almost no FRCs^{ΔTLN1} showed a nuclear localization
286 both under homeostatic and reactive conditions (Figure 7B,C). This finding demonstrates
287 that Talin1 dependent mechanotransduction in FRCs is rate-limiting for YAP/TAZ nuclear
288 translocation and strongly indicate that FRCs^{ΔTLN1} lose their mechanosensitivity. To assess

289 the functional consequences for FRC network integrity we performed *in situ* network
290 analysis. To this end, 3D volumes of FRC networks were acquired from cleared thick
291 vibratome slices and network spacing was quantified using a 3D sphere-filling algorithm
292 (Figure 7D,E). In agreement with the previous 2D GAP analysis (Figure 2) the network of
293 control mice widened and remained intact at D4 of inflammation. The FRC^{ΔTLN1} network
294 under homeostatic conditions was widened compared to controls, but structurally intact.
295 Upon immunization the FRC^{ΔTLN1} network integrity became severely compromised, showing
296 large FRC-free gaps (Figure 7D,E & S4E). These defects were most apparent at D4 and partly
297 recovered by D14 of inflammation.

298 These data suggest that the FRC network in FRC^{ΔTLN1} mice failed to adapt to organ swelling
299 and partly disintegrated or ruptured. To investigate the fate of FRCs under these conditions
300 thick vibratome sections were stained for cleaved caspase 3 (cC3) and Ki67, to identify
301 apoptotic and proliferating FRCs, respectively (Figure 7F,G). These analyses showed little
302 apoptotic and proliferating FRCs in FRC^{ΔTLN1} and control mice under homeostatic conditions.
303 At D4 after immunization, the number of apoptotic FRCs per volume increased significantly
304 in FRC^{ΔTLN1} mice as compared to controls, while proliferation was similar in both control and
305 knockout. At D8, apoptotic FRCs per volume unit were still larger in FRC^{ΔTLN1} compared to
306 controls and proliferating FRCs were increased (Figure 7F,G).

307 These data indicate that compromised mechanosensing causes a severe dysregulation in
308 survival and proliferation of the FRC compartment, which leads to a loss of network
309 integrity. This finding is line with the idea that FRC remodeling is locally controlled by
310 mechanical feedback.

311

312 **Capsule fibrosis constrains lymph nodes at late time points**

313 Network analysis and tension measurements indicated that the FRC network reached a
314 “new equilibrium” two weeks after immunization, because it adopted its homeostatic
315 configuration. Nevertheless, effective resistance remained high at these late time points,
316 raising the question if another structure contributes to the force balance.

317 The LN capsule can be divided into two components: a floor that includes floor lymphatic
318 endothelial cells (fLECs) along with a basement membrane that connects to conduits, and a
319 roof that consists of ECM with embedded lymphoid fibroblasts to which ceiling lymphatic

320 endothelial cells (cLECs) adhere. We investigated the structural and mechanical properties
321 of the two capsule components in homeostatic and inflammatory conditions.
322 fLECs are sparsely labeled in FRC-mTmG mice, as is demonstrated by their double positivity
323 for mGFP and LYVE-1, and their location in the floor of the subcapsular sinus (SCS) (Figure
324 S5A). Since the SCS floor is densely populated by fLECs, we used this sparse labeling to our
325 advantage as it enabled the measurement of active tension on single fLECs *in vivo* using UV-
326 laser ablation (Figure 8A). We found that fLECs had high levels of basal tension that
327 exceeded those of FRCs (Figure 8B). Interestingly, after two days of inflammation fLECs
328 showed reduced tension that was reverted to homeostatic levels in the further swelling
329 phase. Likewise, no rise in active tension on the long time scale (D8-D14) was found on the
330 capsule ECM following UV laser ablation of explanted popliteal LNs (Figure S5B,C).
331 The absence of a continuous rise in active tension on the capsule floor and roof entails that
332 these components are being remodeled to keep up with the volumetric increase of the
333 swelling LN. The capsule was therefore assessed by histology in Prospero homeobox protein
334 1 (Prox1)- GFP mice in which the cytoplasm of all LECs is labeled with GFP. Additional 4',6-
335 diamidino-2-phenylindole (DAPI) and platelet-derived growth factor receptor- β (PDGFR- β)
336 staining allowed the measurement of capsule thickness and mesenchymal cell layers of the
337 capsule above the SCS in homeostasis and inflammation. We found that the capsule
338 thickness remained unchanged in the first four days of inflammation. Strikingly, the capsule
339 thickness increased ~14-fold from D8 to D14 of inflammation, forming a dense fibrotic layer
340 between the parenchyma and surrounding adipose and muscle tissue, while the SCS
341 remained intact (Figure 8C,D & Figure S5D).
342 We asked if such significant remodeling of the capsule resulted in changes in its mechanical
343 properties. To this end a micro-pipette with a small diameter was used to locally aspirate
344 ERTR7 labeled capsules of popliteal LN explants. Using Laplace's law, an effective Young's
345 modulus of the capsule was derived (Figure 8E). We found that the elastic modulus of the
346 capsule remained stable over the first eight days of inflammation but was doubled at D14
347 (Figure 8F). By multiplying the capsule thickness and Young's modulus of the capsule, we
348 derived the passive capsule tension; a measure of the amount of force necessary to enlarge
349 the whole thickness of the capsule by a certain length, i.e. the force needed to swell the LN.
350 The passive tension showed a substantive increase from D0 to D8 of inflammation and kept
351 rising to a massive 150-fold increase at D14 of inflammation (Figure 8G).

352 These data indicate that during a sustained immune response, tension dissipates from the
353 remodeling FRC network at the intermediary time scale (D4-D14), while the capsule
354 remodels and becomes thicker, stiffer and more resistant to swelling at the long time scale
355 (D8-D14), establishing a new force-equilibrium within the organ that resists further swelling
356 (Figure 8H).
357

358 **Discussion**

359 Like glia cells of the nervous system, lymphatic stroma cells were long considered the
360 passive structural elements of the immune system. Only the last two decades revealed that
361 the stromal compartment decisively orchestrates immune cell encounters by providing
362 trophic and tactic cues and that in turn stromal cells dynamically respond to signals
363 provided by the immune cells^{18,19}. Despite palpation of reactive LNs being part of every
364 physical exam and LNs being unmatched in their ability to change volume, the mechanical
365 aspects of LN swelling have never been directly addressed. By measuring organ mechanics
366 across different time and size scales we establish that reactive swelling of the LN is a multi-
367 tier process controlled by mechanical feedback. This allows the organ to expand in a step-
368 wise controlled fashion, without compromising its delicate architecture.

369 We demonstrate that upon inflammation, accumulating lymphocytes inflate the node and
370 initially stretch the FRC network. This is in line with previous findings that FRCs show an
371 early and transient increase in cell size²⁰. Stretching puts tension on the ECM conduit as
372 revealed by a straightened configuration of its ECM fibrils. Although our ultrastructural
373 analysis did not show obvious ruptures of fibrillar collagen, Martinez et al.⁴⁵ detected gaps
374 in the ECM (but not the cellular) compartment of swelling LNs, raising the possibility that in
375 some areas of the LN, flexibility of the ECM cannot keep up with cellular deformation.
376 Interestingly, both our laser cutting experiments and the kinetics of nuclear shuttling of
377 YAP/TAZ revealed that compared to their ECM conduit, FRCs experience cytoskeletal
378 tension only with a time delay of two days. This is well in line with findings of the labs of
379 Turley and Reis e Sousa, who showed that early LN swelling is accompanied by a relaxation
380 of the FRC system, allowing the network to stretch^{22,23}. Mechanistically, they demonstrated
381 that CLEC-2 ligand expressed on activated DCs binds podoplanin on FRCs and that this
382 interaction relaxes actomyosin contractility within the FRC myofibroblastic network. Such a
383 transient FRC relaxation explains why tension-increase of the ECM conduit precedes
384 tension-increase of FRCs and implies that the FRC cytoskeleton only experiences significant
385 tension once the DC-mediated relaxation signals fade after three to four days. Accordingly,
386 FRCs show increased α SMA expression only after the initial days of inflammation²⁰.

387 While the FRC network uses its intrinsic pliability to accommodate short-term volumetric
388 changes, sustained strain on the FRC cytoskeleton triggers the next stage of LN swelling,
389 which is characterized by actual growth and structural remodeling of the network. Our

390 results on genetic ablation of Talin1 in FRCs strongly support the idea that adhesion-
391 dependent mechanosensing is a critical feedback parameter that locally controls growth and
392 survival of the network, so that it reverts to its typical geometry, while being increased in
393 size. In line with these results, mice with a gain of function mutation in the
394 mechanosensitive YAP/TAZ pathway show fibrotic LNs with impaired FRC differentiation⁴⁶
395 and blockade of β 1 integrin triggered FRC apoptosis in swelling (but not in homeostatic)
396 LNs⁴⁷. A critical prerequisite of a model where FRC mechanosensing locally controls network
397 remodeling is that the FRC responsiveness is not restricted to specific niches but rather
398 distributed throughout the organ. Our clonal analyses show that this is indeed the case and
399 match results in follicular dendritic cells and marginal reticular cells that were also shown to
400 undergo clonal expansion⁴⁸.

401 Beyond a week of structural adaptation the FRC network of the now massively enlarged LN
402 seemed to reach a new “mechanical equilibrium” as indicated by gap analysis, ECM
403 alignment, tension measurements and YAP/TAZ translocation. Nevertheless, bulk
404 mechanical properties of the LN did not return to homeostatic levels. They rather showed
405 an elevated effective resistance, indicating that another structure now countered the
406 internal pressure generated by the trapped lymphocytes. We thus turned to the capsule as
407 the second major stromal element and found that during these late stages, thickness and
408 mechanical strength of the capsule were massively increased, explaining resistance to
409 further organ expansion. Although capsule fibrosis is a characteristic histopathological
410 descriptor of reactive LNs⁴⁹, its mechanistic contributions are completely unexplored and
411 future studies will hopefully show how it contributes to sustained or chronic immune
412 responses.

413 As the multi-tier model of LN swelling moves through a succession of check-points, it has
414 the advantage of being adaptable to very different types of swelling-scenarios. Transient
415 swelling, as it occurs e.g. during circadian fluctuations, might stretch the network, but is
416 unlikely to cause structural remodeling. In contrary, sustained immune responses with
417 massive lymphocyte trapping and germinal center reactions, might rely on a fibrotic
418 strengthening of the capsule in order to limit excessive expansion of the organ.

419

420 **Methods**

421

422 **Animals**

423 All animal experiments are in accordance with the Austrian law for animal experiments.
424 Permission was granted by the Austrian Federal Ministry of Science, Research and Economy
425 (identification code: BMWFW 66.018/0010-WF/V/3b/2016). Mice were bred and
426 maintained at the local animal facility in accordance IST Austria Ethical Committee or
427 purchased from Charles River and maintained at the local animal facility in accordance with
428 IST Austria Ethical Committee. OT-II (Stock No: 004194) was bought from JAX. Ccl19-Cre
429 mice have been described previously³². MADM-7³⁹ and Talin1floxed⁵⁰ mice were provided
430 by Simon Hippenmeyer and David Critchley, respectively. All mice are on a C57BL/6J
431 background, with exception of MADM-7 which have a CD-1 background. Mice of both sexes
432 between the age of 6 to 20 weeks were used for experiments. For immunization, KLH
433 protein was dissolved in PBS to 5 mg/mL of and then mixed 1:1 with CFA (both Sigma-
434 Aldrich) upon which 40 μ L of the immunization mixture was injected in footpads and flanks
435 of draining popliteal and inguinal LNS. LNs were harvested after various timepoint up to
436 two weeks of induction of immunization to be used for histology or explant experiments, or
437 used for *in vivo* imaging experiments. For LN cellularity manipulation experiments, mice
438 were i.v. injected with 100 μ g α -CD62L (MEL14) (BioXCell), and control mice with PBS alone.
439 For steady-state evaluation, LNs were harvested 24h after injections were given, and for
440 inflammation conditions injections were given at onset of inflammation. Mice were
441 anesthetized by isoflurane inhalation (IsoFlo, Abbott) for all injection-based experiments, or
442 anaesthetized with a ketamine/xylazine/acepromazine mixture for *in vivo* imaging
443 experiments.

444

445 **Histology and Imaging**

446 LNs were fixed in 4% paraformaldehyde (Electron Microscopy Sciences) in PB (0.1 M, pH 7.4)
447 at 4°C overnight. For cryosections, tissues were additionally embedded for 24h in a solution
448 of 30% glucose in PB (0.1 M, pH 7.4) before embedding and freezing in Tissue-Tek optimum
449 cutting temperature (OCT) compound (Sakura). Cryostat section (10-12 μ m) were collected
450 on Superfrost/Plus glass slides (Thermo Fisher Scientific). Alternatively fixed tissues were

451 embedded in 4% low melting temperature agarose (Invitrogen) after fixation and 100-400
452 μm sections were cut using a vibratome (VT1200S, Leica Microsystems).

453

454 Cryostat sections were air-dried for 2h at room temperature (RT) and washed in PBS.
455 Sections were blocked in SEABLOCK blocking buffer (Thermo Fisher Scientific) or in 5%
456 bovine serum albumin (BSA) (Thermo Fisher Scientific) in PBS for 1h, followed by incubation
457 of primary antibody solution diluted in 1% BSA/PBS for 1.5h at RT, 3 washing steps in PBS
458 and subsequent incubation of secondary antibody solution diluted in 1%BSA/PBS for 30 min
459 at RT. Finally, sections were washed three times in PBS, air-dried and mounted using
460 Fluoromount-G with DAPI (Thermo Fisher Scientific). Vibratome sections were blocked in 5%
461 BSA/0.3%Triton-x/PBS for 2h at RT under agitation followed by primary antibody incubation
462 in 1% BSA/0.3%Triton-x/PBS overnight at 4°C under agitation or for 2 days at RT in some
463 cases. The following day sections were washed three times in PBS. In case primary
464 antibodies were not conjugated with a fluorescent dye, samples were incubated with a
465 secondary antibody in 1% BSA/0.3%Triton-x/PBS for 4h at RT under mild agitation and
466 subsequently washed three times in PBS. All samples were then incubated in DAPI solution
467 for 15 min and mounted on a glass slide using Fluoromount-G (Thermo Fisher Scientific).
468 The following primary antibodies were used: α -CD3 ϵ AF488 (17A2)(eBioscience), α -B220-
469 Biotin (RA3-6B2) (eBioscience), α -Collagen IV-Biotin (Abcam), α -CCL21-Biotin (R&D Systems),
470 α -PDPN-Biotin (8.1.1) (eBioscience), α -PDGFR- β (R&D Systems), α -YAP/TAZ (D24E4) (Cell
471 Signal), α -cleaved Caspase 3-AF647 (Asp175) (Cell Signal), α -Ki67-APC (SolA15)
472 (eBioscience), α -ICAM-1 (YN1/1.7.4) (BioXCell), α -VCAM-1 (Phe25-Glu698) (R&D Systems),
473 α -Fibroblast Marker-AF647 (ERTR7) (Santacruz Biotech). α -PNAd (MECA-79) was derived
474 from a concentrated hybridoma supernatant (kind gift from Christine Moussion). The
475 following secondary antibodies were used: Streptavidin-Cy3 (Sigma-Aldrich), Streptavidin-
476 AF647 (Jackson ImmunoResearch), chicken α -goat AF488 (Invitrogen), donkey α -rat AF647
477 (Jackson ImmunoResearch), donkey α -rabbit AF647 (Jackson ImmunoResearch), goat α -
478 mouse IgM AF647 (Invitrogen). Images were acquired on a Zeiss LSM800 inverted confocal
479 laser scanning microscope (CLSM) with the following objectives: 10x/NA0.45, 20x/NA0.8,
480 40x/NA1.2 Water and 63x/NA1.4 Oil Plan-APOCHROMAT.

481 Thick vibratome sections were in some cases cleared using the Ce3D protocol as described
482 previously⁵¹. Briefly, following antibody-staining samples were washed at RT on a shaker for
483 8h in washing buffer (PBS/0.3% Triton X-100, 0.5% 1-thioglycerol) which was refreshed after
484 4h. Next samples were cleared in freshly prepared Ce3D solution for 2x 1h, mounted in a μ -
485 dishes (Ibidi) and submerged in Ce3D solution. A cover-glass was placed on top to mount
486 cleared samples to the bottom of the well and the dish sealed with parafilm. Large 3D
487 volumes (xy:306x306 μ m, z: 50-300 μ m) were acquired from Ce3D cleared thick vibratome
488 sections using a spinning-disc microscope (Dragonfly, Andor) with a Aplanachromat LWD λ S
489 40x/1.15 Water 0.60 mm WD objective.

490 **3D LSFM Sample Preparation and Imaging**

491 Terminally anesthetized Ccl19-cre hem; MADM-7^{GT/TG} mice (mix C57BL/6J and CD1
492 background) were *in vivo* stained by retro-orbital injection of 40 μ g/PBS mouse α -peripheral
493 node addressin (PNA_d) concentrated hybridoma supernatant labeled with Atto-647N-NHS
494 (Atto-Tec). After 10 min, popliteal LNs were harvested and fixed in 4% paraformaldehyde
495 (Electron Microscopy Sciences) overnight at 4°C. Samples were washed in PBS, cleaned
496 under a stereomicroscope and cleared with the CUBIC protocol⁵². Briefly, samples were
497 incubated in CUBIC reagent 1 for 3 days at 37°C, which was replaced every 24h. Samples
498 were then washed with PBS, embedded in 2% low-melting temperature agarose (Sigma-
499 Aldrich), and sequentially dehydrated in 30% sucrose (Sigma-Aldrich) (1 day at 4°C) and 50%
500 sucrose (2 days at 4°C). Finally, samples were incubated in CUBIC reagent 2 for 2 days at RT.
501 Cleared samples were imaged using a custom LSFM setup⁵³. Acquired images were stitched
502 using the FIJI Grid/Collection-stitching plugin (Preibitsch Laboratory), despeckled and
503 manually registered using a custom-alignment-tool in Matlab (developed by Ekaterina
504 Papusheva).

505

506 **FRC Cluster Analysis**

507 MADM-labeled cells were detected in 3D by employing a spot detection algorithm (Bitplane
508 Imaris) for each channel (tdTomato & GFP) separately. Chromatic aberrations and the
509 sequential nature of the image acquisition led to a channel misalignment which was
510 corrected for in the following way: the spot coordinates were exported from Imaris and
511 treated as a point cloud for each channel. These point clouds were then registered onto

512 each other using the Iterative closest point algorithm which corrected the shift and the
513 rotation of the spectral channels. Cells were then sorted into color classes (green (GFP), red
514 (tdTomato) or yellow (double positive) lineage). Red or green, if the spot existed solely in
515 one of the point clouds, or yellow if there were two corresponding spots in both channels
516 that are closer than the typical cell radius.

517

518 For the cluster analysis the LN outline and the HEVs were segmented in Imaris using the
519 surface detection feature. To correct errors in the cell detection, falsely detected spots from
520 autofluorescent structures outside of the LN volume were excluded from further analysis. In
521 order to avoid edge effects cells in a region 100 μm from the surface of the analyzed LNs
522 were excluded. FRC clusters were analyzed using a custom Matlab script utilizing a density-
523 based spatial clustering of applications with noise (DBSCAN) algorithm⁴⁰ in which FRCs were
524 represented as 3D spheres with a 12 μm diameter. An FRC cluster was defined as a
525 minimum of three FRCs of the same lineage (green or red) within a search-radius of 20 μm
526 from each FRC-sphere's surface.

527

528 To generate a random distribution (simulated FRCs), FRC-spheres were placed into the same
529 volume occupied by the real cells and excluded from HEV volumes. For each timepoint the
530 average of 10 distributions was used. The *cluster factor (CF)* was defined as *FRCs in*
531 *clusters/Total number of FRCs* divided by *Simulated FRCs in clusters/Total number of*
532 *simulated FRCs*.

533

534 **FRC Network GAP Analysis**

535 2D: A confocal laser scanning microscope with a 40x 1.2 water-objective (LSM800, Zeiss)
536 was used to acquire image stacks (range 10-30 μm and spaced at 1 μm) with a field of view
537 of 240x240 μm and a pixel size of 0.5 μm from T zones in which FRCs were labeled by mGFP
538 (Ccl19-Cre; mTmG mice). These were subsequently segmented using Ilastik software, the
539 result was then transformed into a binary image and noise was removed using a custom FIJI
540 script that utilized the particle detection algorithm. Binarized 3D image-stacks were then
541 used to measure the spacing (gaps) in the network by analyzing the pore-size distribution on
542 individual z-sections. The pore-size distribution was obtained analogously to the pore-size
543 analysis described in *Acton et al.*²². Starting with a circle size which corresponded to the

544 maximum gap of the network, circles were consecutively positioned into fitting
545 corresponding gaps of the network. The maximum circle size was determined from a
546 distance transform of the segmented network. Once no more circles of the maximum size
547 could be placed into gaps of the network, the disk size was reduced by one unit and the
548 placement of the disks of reduced sized commenced. This way, the gaps in the network
549 were consecutively filled with circles of decreasing size until the entirety of the gap area was
550 filled. The results were then averaged over the

551 3D: Large 3D volumes (xy:306x306 μm , z:50-500 μm) were acquired from Ce3D⁵¹ cleared
552 thick vibratome sections using a Apochromat LWD λS 40x/1.15 Water 0.60 mm WD
553 objective on a spinning disc microscope (Dragonfly, Andor). Acquired 3D stacks were
554 corrected for fluorescent intensity in z-axis using 'bleach correction (histogram matching)'
555 function in Fiji. Imaris was then used to generate a 3D binary image of the FRC network by
556 utilizing a surface detection feature from the FRC-network fluorescent channel. A custom
557 Matlab script was subsequently used to fit 3D spheres in the 3D gaps of the network analog
558 to the 2D approach.

559

560 **Parallel Plate Compression Experiments**

561 Explanted popliteal LNs were cleaned from adipose tissue under a stereomicroscope and
562 placed on a glass plate within the 37°C, RPMI 1640 (Invitrogen) filled incubation chamber of
563 a MicroSquisher device (CellScale). LNs were oriented to have their long axis along the field
564 of view of the camera. Compression was performed with a glass plate glued onto either a
565 0.304 or 0.408 mm diameter 40 GPa tungsten filament with a length of 60 mm. The glass
566 slide on the compression probe was coated with Poly-HEMA (Sigma-Aldrich) to reduce
567 sticking of the samples. LNs were then compressed by 25% of the initial height by lowering
568 the upper plate down in a timespan of 30 seconds. Lateral side-views of LNs were recorded
569 up to 20-60 min after onset of the experiment, while resistant forces were measured on the
570 upper plate. Compression protocols, images and force acquisition were realized with the
571 SquisherJoy software (CellScale). Length, height, contact area and curvature of LNs were
572 manually measured before compression, and at the equilibrium timepoints using Fiji
573 software. The recorded compression force together with the measured geometrical
574 parameters were used to calculate volumes, Young's modulus, effective resistance and
575 viscosity using a generalized Kelvin model²⁷. This was done as following:

576 The force required to maintain a constant strain of 25% on a LN was measured over time
577 (F(t)). The force initially peaks and then follows a relaxation curve which is fitted by a double
578 exponential decay curve. The simplest way to describe this bimodal dynamic is to
579 incorporate two dashpots with constants μ_1 and μ_2 , and two springs with k_1 and k_2
580 constants. After 20-60 min, the system reaches an equilibrium where the exerted force by
581 the plate equals the effective resistance of the LN (σ). Therefore, we have:

$$\sigma = \frac{F_{eq}/\pi R_3^2}{(1/R_1 + 1/R_2)}$$

582 where F_{eq} is the equilibrium force at steady state and R_1 , R_2 and R_3 are derived from the
583 geometry of the LN.

584 To obtain the elastic modulus, the stress and strain need to be acquired:

585 Stress (s) is calculated from the force at equilibrium divided by plate contact area:

$$s = F_{eq}/\pi R_3^2$$

586 and the strain (ε) from:

$$\varepsilon = 1 - \frac{h_{eq}}{h_0}$$

587 where h_0 and h_{eq} correspond to the initial and equilibrium height of the compressed LN.

588 From here the elastic modulus (E) can be derived:

$$E = s/\varepsilon$$

589 Next, by fitting a double exponential decay to the force curve we obtain two time-scales, τ_1
590 and τ_2 , where:

$$\tau_i = \mu_i/k_i, i = 1, 2$$

591 Following up on the derivations of the equations as in *Forgacs et al.*²⁷, μ_1 and μ_2 can be
592 acquired readily, where μ_1 corresponds to the initial fast response in the order of seconds
593 and μ_2 to the slower response in the order of minutes, of which the latter one becomes
594 relevant for the rearrangements of the cells within LNs. Hence, we use μ_2 as our viscosity.

595 Measurements in which the LN was damaged during preparation (lymphocytes leaking out)
596 or moved/rolled during compression were excluded. In a few cases the viscosity could not
597 be determined (infinitely small) and were also excluded.

598 LN volumes were calculated from side-view images at $t=0$ with the following formula:

$$V = \frac{4}{3} \pi R_1 \left(\frac{h_0}{2}\right)^2$$

599

600 **Micropipette Assay**

601 Popliteal LN explants were cleared from fat and incubated for 10 min in a 2 µg/mL ERTR7-
602 AF647 (Santa-Cruz) in RPMI 1640 (Invitrogen) to label the capsule. LNs were subsequently
603 placed on 3% methylcellulose coated glass bottom Petri dishes (MatTek) in RPMI and kept
604 at 37°C, while imaged on an inverted Leica SP5 microscope using a 20x, 0.7NA objective
605 (Leica Microsystems). The local Young's Modulus of the capsule was measured with a glass
606 micropipette connected to a Microfluidic Flow Control System (Fluigent, Fluiwell), with
607 negative pressure ranging from 7-750 Pa, a pressure accuracy of 7 Pa and change rate of
608 200 Pa*s⁻¹. The micropipette equipment was mounted on a motorized micromanipulator
609 (Eppendorf, Transferman Nk2). Both systems were controlled by Dikeria software, Labview
610 (National Instruments). A fire polished micropipette with an inner diameter of 15 µm and
611 flat end (BioMedical instruments) was used for aspiration. The chosen diameter ensured
612 that mainly the capsule was probed and not the underlying parenchyma. While localizing
613 the LN capsule with the micropipette, the pressure inside the micropipette was kept at 0 Pa.
614 For measurements, a negative pressure of 750 Pa was applied, which resulted in the
615 instantaneous aspiration of the capsule. This pressure was chosen as lower pressure
616 regimes did not result in proper aspiration of the capsule. The tongue length of the capsule
617 in the micropipette upon aspiration was manually measured in Fiji from acquired movies.
618 The elasticity was subsequently calculated using the Laplace law:

$$E = \frac{\Delta P}{\left(\frac{h}{d}\right)^2}$$

619 With ΔP being the pressure difference between micropipette and atmosphere, h the height
620 of the measured tongue, and d the micropipette diameter.

621

622 **SEM Sample Preparation and Imaging**

623 Terminally ketamine/xylazine/acepromazine anesthetized mice were transcardially perfused
624 with PB (0.1 M, pH 7.4) and subsequently fixed with 2.5% glutaraldehyde and 2%
625 paraformaldehyde (Science Services) in PB (0.1 M, pH 7.4). LN samples were then dissected
626 and post-fixed in the same buffer for another hour at RT. They were dehydrated in a graded
627 ethanol series of 50%, 70%, 90%, 96%, 100% in H₂O for a minimum of 10 min per step and

628 subsequently kept overnight in fresh 100% ethanol at 4°C. Once in 100% ethanol, samples
629 were dried with a critical point dryer (EM-CPD300, Leica Microsystems), cut in half and
630 coated with a 4nm layer of platinum using a sputter coater (EM-ACE600, Leica
631 Microsystems). The samples were imaged with a field emission scanning electron
632 microscope Merlin compact VP (Carl Zeiss) at 3 kV. The signal was detected by an Everhart-
633 Thornley type secondary electron detector.

634

635 **STEM Tomography Sample Preparation**

636 Alkali maceration of LNs was performed as previously described^{54,55}. Briefly, popliteal LNs
637 were isolated from 8–12 weeks old wt C57BL/6 mice and directly fixed in a 2.5%
638 glutaraldehyde and 2% paraformaldehyde in PB (0.1 M, pH 7.4) for a minimum of two weeks
639 at 4°C. Samples were then macerated in aqueous 2.5 M (10% w/v) NaOH solution for 5 days
640 at RT under mild agitation. Next sections were rinsed in H₂O under mild agitation for one to
641 two days until samples became pale. If results were not sufficient, the maceration step was
642 repeated.

643

644 Samples were then treated with 0.5% tannic acid (w/v) in PB (0.1 M, pH 7.4) two times 1h
645 each with freshly prepared solutions, washed in PB and treated with aqueous 1% osmium
646 tetroxide (w/v) for 30 min at 4°C. Samples were contrast enhanced with aqueous 1% uranyl
647 acetate (w/v) overnight at 4°C and Walton's lead aspartate for 30 min at 60°C. Samples
648 were then dehydrated in graded ethanol, infiltrated with anhydrous propylene oxide and
649 embedded in hard-grade epoxy resin (Durcupan® ACM, Fluca). Samples were consecutively
650 infiltrated with a 3:1 mixture of anhydrous acetone and Durcupan® for 1h at 4°C, 1:1
651 acetone/Durcupan® for 1.5h at 4°C, 1:3 acetone/Durcupan® for 2h at 4°C and mere Durcupan®
652 overnight at RT. Samples were transferred to BEEM capsules (Electron Microscopy
653 Sciences), filled with freshly prepared Durcupan® and cured for 48h at 60°C.

654

655 **STEM Tomography Imaging**

656 Semi-thin sections were cut at 450 nm using an UC7 ultramicrotome (Leica Microsystems)
657 and collected onto formvar-coated 200-line bar grids + 1C/bar (Science Services, G200PB)
658 and coated with evaporated carbon to a thickness of 8nm. Grids were cut in half, mounted
659 on a Half-Mesh High Tilt holder (Jeol, EM-21010/Z09291THTR) and observed under a JEM

660 2800 scanning transmission electron microscope (Jeol) operated at 200 kV in STEM mode.
661 To compensate for focus, contrast and brightness, and stage shift during image tilt series
662 recording, an automated system was used comprising the STEM Recorder V3 Vers. 3.2.8.0
663 and the STEM Magica Controller Vers. 0.9.8.1 (both System In Frontier Inc.). Images were
664 collected at 2° intervals between +/-76° of single tilt axis. Magnification was x80k – x600k,
665 image size 512x512 pixels giving a pixel sizes from 6.749463 nm/px to 0.899928 nm/px.

666

667 **Conduit Stretching Quantification**

668 STEM Tomography images were aligned by cross-correlation and 3D structure of area of
669 interest computed by weighted back-projection using Composer software Vers. 3.0 (System
670 In Frontier Inc.). A 3D Gaussian blur filter and background subtraction (rolling ball algorithm)
671 pre-processing step were performed on the images using FIJI. The 3D image stacks were
672 subsequently loaded into Imaris, and fibrils of conduits were manually traced using the
673 Filament Tracer tool and exported to Matlab format using the Object Exporter (exported
674 from Imaris as filaments). The overall orientation and curvature of the centerline of the
675 entire conduit was approximated by fitting a cubic spline curve with four support points
676 which minimized a hand-crafted cost function through all fibril track data. This cost function
677 penalizes the distance of the desired centerline to the tracks, the total curvature of the
678 centerline and the difference in length between it and the fibril bundles, and ensures that
679 the support points are spaced evenly. In a few cases this spline curve was corrected by hand
680 if it was found to not adequately represent the center line of the bundle. The alignment of
681 the individual fibrils with respect to the centerline of the conduit was calculated as follows:
682 The spline centerline was interpolated in a continuous fashion and the 3D orientation was
683 calculated. Likewise, the tracks of individual fibrils were first smoothed to reduce tracing
684 errors and the 3D orientation of each segment of the trace was calculated. The alignment
685 angle A between the fibril is then given by the angle between the orientation of the
686 segment and the orientation of the centerline at the point that is closest to the segment:

687

$$A = \text{acos} \left(\text{abs} \left(\frac{\vec{v}_{fibril} \cdot \vec{v}_{Centerline}}{|\vec{v}_{fibril}| \times |\vec{v}_{Centerline}|} \right) \right)$$

688

689 **UV-Laser Cutter Setup**

690 The UV-laser cutter setup is based on a previously described layout^{35,56}. In brief, a passively
691 Q-switched solid-state 355 nm UV-A laser (Powerchip, Teem Photonics) with a repetition
692 rate of 1 kHz, pulse energy of 15 μ J, pulse-length of <350 ps and peak-power of 40 kW was
693 used in conjugation with a spinning disc microscope (Axio Observer Z1, Zeiss). The system is
694 controlled using custom-built software (LabView, National Instruments) enabling cutting in
695 3D. Typically 5% of the power is used to cut tissues.

696

697 **UV-Laser Ablation Experiments**

698 Tension on FRCs, fLECs and capsule ECM was measured by conducting laser ablations on an
699 inverted UV-laser ablation setup with a manufacturer 40x 1.2NA water immersion lens in
700 homeostatic and inflamed LNs. For all experiments 25 UV pulses at 1000 Hz to 40
701 equidistant sites using 200 ms exposure time and frame rate were used to ablate and
702 capture tissue recoil. For FRC and LEC ablation, we established an intravital setup where
703 Ccl19-Cre hem; mTmG hom mice were anesthetized and intact inguinal LNs exposed using a
704 skin flap surgery. The paracortical site of the LN was mounted on a custom-made stage
705 which allowed the LN temperature to be regulated at 37°C. For capsule ECM ablation,
706 popliteal LNs were harvested and incubated in 100 μ M TAMRA in RPMI 1640 solution (both
707 Invitrogen) for 15 min at RT and directly used for experiments. Explanted LNs were mounted
708 at room temperature in a glass bottom Petri dish (MatTek) in RPMI and prevented from
709 floating using a 22x22 mm cover glass topping.

710 Cuts were performed in either three z-planes spaced 1 μ m apart along a length of either 10
711 μ m for FRCs, or in one z-plane along 20 μ m for fLECs and capsule ECM. FRC cuts were
712 typically performed at 10-20 μ m depth underneath the capsule. Recoil of FRCs and LECs was
713 quantified from kymographs made in FIJI, while capsule ECM recoil was quantified using
714 PIVlab in Matlab. In the latter case, temporal recoil velocities were measured between
715 bandpass filtered pre- and consecutive post-cut frames by averaging the component of the
716 calculated velocity in the perpendicular direction to the cut, within an area of the
717 surrounding cut site.

718

719 **YAP/TAZ Quantification**

720 The nuclear to cytoplasmic ration of stained YAP/TAZ in FRCs were measured from 3D
721 sections of peripheral LNs. In FIJI, FRCs were identified by the mGFP labeling and for each
722 FRC the average YAP/TAZ fluorescent intensity of the nucleus (identified by DAPI) was
723 divided by the average intensity of the adjacent cytoplasm of the cell body. In other cases,
724 YAP/TAZ localization was qualitatively assessed to contain to either contain a higher nuclear
725 or cytoplasmic YAP/TAZ intensity.

726

727 **CCL21 Quantification**

728 Cryosections containing both a control and FRC^{ATLN1} peripheral LN in a single section were
729 stained for CCL21 and pair-wise imaged using similar settings. The average fluorescent
730 intensities of CCL21 were then measured from paracortical areas and normalized to the
731 control.

732

733 **Proliferation and Apoptosis Measurements of FRCs**

734 Large 3D volumes (xy:306x306 μm , z: 50-150 μm) stained for either cleaved Caspase 3 or
735 Ki67 were acquired from Ce3D cleared thick vibratome sections were corrected for
736 fluorescent intensity in z-axis using 'bleach correction (histogram matching)' function in Fiji.
737 Imaris was then used to generate a 3D isosurface of the FRC network by utilizing a surface
738 detection feature from the FRC-network fluorescent channel. The isosurface was then used
739 to mask the cleaved Caspase 3 and Ki67 channels so only the fluorescent signal within the
740 FRC network remained. Positive nuclei were then manually counted from 2D slice views and
741 normalized for per volume unit.

742

743 **Capsule Thickness Measurements**

744 The thickness of capsules was measured in vibratome sections of PROX1-GFP or wt mice,
745 stained for PDGFR- β and DAPI. The size of the capsule was then manually measured in FIJI
746 from the SCS to the surrounding adipose or muscular tissue from at least 3 locations and
747 were averaged per LN.

748

749 **Statistical Analysis**

750 All statistical analyses were performed in GraphPad Prism 8. P-values <0.05 were considered
751 significant.

752

753 **Software**

FIJI	Schindelin et al., 2012	https://fiji.sc/
Imaris	Bitplane	https://imaris.oxinst.com/packages
Excel	Microsoft	https://products.office.com/en-us/?rtc=1
Prism	GraphPad Software	https://www.graphpad.com/scientific-software/prism/
MATLAB	MATLAB Software	https://www.mathworks.com/products/matlab.html
Ilastik	Sommer et al., 2011	https://www.ilastik.org/
SquisherJoy	Cell Scale	https://www.cellscale.com/products/microtester/
Composer software	System In Frontier Inc.	https://temography.com/en/composer-en/
PIVlab	Thielicke and Stamhuis 2014	https://pivlab.blogspot.com/

754

755 **Data availability**

756 Data supporting the findings of this study are available from the corresponding
757 authors upon.

758

759 **Code availability**

760 Code used for various analyses in this study are available from the
761 corresponding authors upon request.

References

762

763 1. Lämmermann, T. & Sixt, M. The microanatomy of T-cell responses. *Immunol Rev* **221**, 26–
764 43 (2008).

765 2. Pham, T. H. M., Okada, T., Matloubian, M., Lo, C. G. & Cyster, J. G. S1P1 Receptor
766 Signaling Overrides Retention Mediated by G α i-Coupled Receptors to Promote T Cell Egress.
767 *Immunity* **28**, 122–133 (2008).

768 3. Druzd, D. *et al.* Lymphocyte Circadian Clocks Control Lymph Node Trafficking and
769 Adaptive Immune Responses. *Immunity* **46**, 120–132 (2017).

770 4. Suzuki, K., Hayano, Y., Nakai, A., Furuta, F. & Noda, M. Adrenergic control of the adaptive
771 immune response by diurnal lymphocyte recirculation through lymph nodes. *J Exp Med* **213**,
772 2567–2574 (2016).

773 5. Luther, S. A., Tang, H. L., Hyman, P. L., Farr, A. G. & Cyster, J. G. Coexpression of the
774 chemokines ELC and SLC by T zone stromal cells and deletion of the ELC gene in the plt/plt
775 mouse. *Proc National Acad Sci* **97**, 12694–12699 (2000).

776 6. Matloubian, M. *et al.* Lymphocyte egress from thymus and peripheral lymphoid organs is
777 dependent on S1P receptor 1. *Nature* **427**, 355–360 (2004).

778 7. Mionnet, C. *et al.* High endothelial venules as traffic control points maintaining
779 lymphocyte population homeostasis in lymph nodes. *Blood* **118**, 6115–6122 (2011).

780 8. Andrian, U. H. von & Mempel, T. R. Homing and cellular traffic in lymph nodes. *Nat Rev*
781 *Immunol* **3**, 867–878 (2003).

782 9. Link, A. *et al.* Fibroblastic reticular cells in lymph nodes regulate the homeostasis of naive
783 T cells. *Nat Immunol* **8**, 1255–1265 (2007).

784 10. Knop, L. *et al.* IL-7 derived from lymph node fibroblastic reticular cells is dispensable for
785 naive T cell homeostasis but crucial for central memory T cell survival. *Eur J Immunol* **50**,
786 846–857 (2020).

787 11. Gorelik, L. *et al.* Normal B Cell Homeostasis Requires B Cell Activation Factor Production
788 by Radiation-resistant Cells. *J Exp Medicine* **198**, 937–945 (2003).

789 12. Cremasco, V. *et al.* B cell homeostasis and follicle confines are governed by fibroblastic
790 reticular cells. *Nat Immunol* **15**, 973–981 (2014).

791 13. Nakai, A., Hayano, Y., Furuta, F., Noda, M. & Suzuki, K. Control of lymphocyte egress
792 from lymph nodes through β 2-adrenergic receptors. *J Exp Med* **211**, 2583–2598 (2014).

- 793 14. Devi, S. *et al.* Adrenergic regulation of the vasculature impairs leukocyte interstitial
794 migration and suppresses immune responses. *Immunity* **54**, 1219-1230.e7 (2021).
- 795 15. Kaldjian, E. P., Gretz, J. E., Anderson, A. O., Shi, Y. & Shaw, S. Spatial and molecular
796 organization of lymph node T cell cortex: a labyrinthine cavity bounded by an epithelium-
797 like monolayer of fibroblastic reticular cells anchored to basement membrane-like
798 extracellular matrix. *Int Immunol* **13**, 1243–1253 (2001).
- 799 16. Sixt, M. *et al.* The Conduit System Transports Soluble Antigens from the Afferent Lymph
800 to Resident Dendritic Cells in the T Cell Area of the Lymph Node. *Immunity* **22**, 19–29 (2005).
- 801 17. Bajénoff, M. *et al.* Stromal Cell Networks Regulate Lymphocyte Entry, Migration, and
802 Territoriality in Lymph Nodes. *Immunity* **25**, 989–1001 (2006).
- 803 18. Perez-Shibayama, C., Gil-Cruz, C. & Ludewig, B. Fibroblastic reticular cells at the nexus of
804 innate and adaptive immune responses. *Immunol Rev* **289**, 31–41 (2019).
- 805 19. Krishnamurty, A. T. & Turley, S. J. Lymph node stromal cells: cartographers of the
806 immune system. *Nat Immunol* **21**, 369–380 (2020).
- 807 20. Yang, C.-Y. *et al.* Trapping of naive lymphocytes triggers rapid growth and remodeling of
808 the fibroblast network in reactive murine lymph nodes. *Proc National Acad Sci* **111**, E109–
809 E118 (2014).
- 810 21. McConnell, I. & Hopkins, J. Lymphocyte traffic through antigen-stimulated lymph nodes.
811 I. Complement activation within lymph nodes initiates cell shutdown. *Immunology* **42**, 217–
812 23 (1981).
- 813 22. Acton, S. E. *et al.* Dendritic cells control fibroblastic reticular network tension and lymph
814 node expansion. *Nature* **514**, 498–502 (2014).
- 815 23. Astarita, J. L. *et al.* The CLEC-2–podoplanin axis controls the contractility of fibroblastic
816 reticular cells and lymph node microarchitecture. *Nat Immunol* **16**, 75–84 (2015).
- 817 24. Chyou, S. *et al.* Coordinated Regulation of Lymph Node Vascular–Stromal Growth First
818 by CD11c+ Cells and Then by T and B Cells. *J Immunol* **187**, 5558–5567 (2011).
- 819 25. Gregory, J. L. *et al.* Infection Programs Sustained Lymphoid Stromal Cell Responses and
820 Shapes Lymph Node Remodeling upon Secondary Challenge. *Cell Reports* **18**, 406–418
821 (2017).
- 822 26. Majumder, S. *et al.* IL-17 metabolically reprograms activated fibroblastic reticular cells
823 for proliferation and survival. *Nat Immunol* **20**, 534–545 (2019).
- 824 27. Forgacs, G., Foty, R. A., Shafir, Y. & Steinberg, M. S. Viscoelastic Properties of Living
825 Embryonic Tissues: a Quantitative Study. *Biophys J* **74**, 2227–2234 (1998).

- 826 28. Delarue, M. *et al.* Self-driven jamming in growing microbial populations. *Nat Phys* **12**,
827 762–766 (2016).
- 828 29. Jain, R. K., Martin, J. D. & Stylianopoulos, T. The Role of Mechanical Forces in Tumor
829 Growth and Therapy. *Annu Rev Biomed Eng* **16**, 321–346 (2014).
- 830 30. Mao, Y. *et al.* Differential proliferation rates generate patterns of mechanical tension
831 that orient tissue growth. *Embo J* **32**, 2790–2803 (2013).
- 832 31. Gallatin, W. M., Weissman, I. L. & Butcher, E. C. A cell-surface molecule involved in
833 organ-specific homing of lymphocytes. *Nature* **304**, 30–34 (1983).
- 834 32. Chai, Q. *et al.* Maturation of Lymph Node Fibroblastic Reticular Cells from
835 Myofibroblastic Precursors Is Critical for Antiviral Immunity. *Immunity* **38**, 1013–1024
836 (2013).
- 837 33. Madisen, L. *et al.* A robust and high-throughput Cre reporting and characterization
838 system for the whole mouse brain. *Nat Neurosci* **13**, 133–140 (2010).
- 839 34. Smutny, M., Behrndt, M., Campinho, P., Ruprecht, V. & Heisenberg, C.-P. Tissue
840 Morphogenesis, Methods and Protocols. *Methods Mol Biology* **1189**, 219–235 (2014).
- 841 35. Colombelli, J., Grill, S. W. & Stelzer, E. H. K. Ultraviolet diffraction limited nanosurgery of
842 live biological tissues. *Rev Sci Instrum* **75**, 472–478 (2004).
- 843 36. Panciera, T., Azzolin, L., Cordenonsi, M. & Piccolo, S. Mechanobiology of YAP and TAZ in
844 physiology and disease. *Nat Rev Mol Cell Bio* **18**, 758–770 (2017).
- 845 37. Zong, H., Espinosa, J. S., Su, H. H., Muzumdar, M. D. & Luo, L. Mosaic Analysis with
846 Double Markers in Mice. *Cell* **121**, 479–492 (2005).
- 847 38. Contreras, X. *et al.* A genome-wide library of MADM mice for single-cell genetic mosaic
848 analysis. *Cell Reports* **35**, 109274 (2021).
- 849 39. Hippenmeyer, S., Johnson, R. L. & Luo, L. Mosaic Analysis with Double Markers Reveals
850 Cell-Type-Specific Paternal Growth Dominance. *Cell Reports* **3**, 960–967 (2013).
- 851 40. Ester, M., Kriegel, H.-P., Sander, J. & Xu, X. A density-based algorithm for discovering
852 clusters in large spatial databases with noise. in *Proceedings of the Second International*
853 *Conference on Knowledge Discovery and Data Mining* (eds. Simoudis, E., Han, J. & Fayyad,
854 U.) 226–231 (AAAI Press, 1996).
- 855 41. Bailey, N. T. J. *The Elements of Stochastic Processes with Applications to the Natural*
856 *Sciences*. (Wiley-Interscience, 1990).
- 857 42. Schaeuble, K. *et al.* Perivascular Fibroblasts of the Developing Spleen Act as LT α 1 β 2-
858 Dependent Precursors of Both T and B Zone Organizer Cells. *Cell Reports* **21**, 2500–2514
859 (2017).

- 860 43. Cheng, H.-W. *et al.* Origin and differentiation trajectories of fibroblastic reticular cells in
861 the splenic white pulp. *Nat Commun* **10**, 1739 (2019).
- 862 44. Austen, K. *et al.* Extracellular rigidity sensing by talin isoform-specific mechanical
863 linkages. *Nat Cell Biol* **17**, 1597–1606 (2015).
- 864 45. Martinez, V. G. *et al.* Fibroblastic Reticular Cells Control Conduit Matrix Deposition
865 during Lymph Node Expansion. *Cell Reports* **29**, 2810-2822.e5 (2019).
- 866 46. Choi, S. Y. *et al.* YAP/TAZ direct commitment and maturation of lymph node fibroblastic
867 reticular cells. *Nat Commun* **11**, 519 (2020).
- 868 47. Kumar, V. *et al.* A Dendritic-Cell-Stromal Axis Maintains Immune Responses in Lymph
869 Nodes. *Immunity* **42**, 719–730 (2015).
- 870 48. Jarjour, M. *et al.* Fate mapping reveals origin and dynamics of lymph node follicular
871 dendritic cells. *J Exp Med* **211**, 1109–1122 (2014).
- 872 49. Mills, S. *Histology for Pathologists*. (LWW, 2019).
- 873 50. Nieswandt, B. *et al.* Loss of talin1 in platelets abrogates integrin activation, platelet
874 aggregation, and thrombus formation in vitro and in vivo. *J Exp Medicine* **204**, 3113–3118
875 (2007).
- 876 51. Li, W., Germain, R. N. & Gerner, M. Y. High-dimensional cell-level analysis of tissues with
877 Ce3D multiplex volume imaging. *Nat Protoc* **14**, 1708–1733 (2019).
- 878 52. Susaki, E. A. *et al.* Whole-Brain Imaging with Single-Cell Resolution Using Chemical
879 Cocktails and Computational Analysis. *Cell* **157**, 726–739 (2014).
- 880 53. Abe, J. *et al.* Light sheet fluorescence microscopy for in situ cell interaction analysis in
881 mouse lymph nodes. *J Immunol Methods* **431**, 1–10 (2016).
- 882 54. OHTANI, O. Three-dimensional Organization of the Connective Tissue Fibers of the
883 Human Pancreas: A Scanning Electron Microscopic Study of NaOH Treated-Tissues. *Arch*
884 *Histol Japon* **50**, 557–566 (1987).
- 885 55. Ushiki, T., Ohtani, O. & Abe, K. Scanning electron microscopic studies of reticular
886 framework in the rat mesenteric lymph node. *Anatomical Rec* **241**, 113–122 (1995).
- 887 56. Behrndt, M. *et al.* Forces Driving Epithelial Spreading in Zebrafish Gastrulation. *Science*
888 **338**, 257–260 (2012).
- 889

Acknowledgements

890 This research was supported by the Scientific Service Units of IST Austria through resources
891 provided by the Bio Imaging, Electron Microscopy, Preclinical and Life Science Facilities. We
892 thank Christine Moussion for providing anti-PNAd antibody, Simon Hippenmeyer and David
893 Critchley for respectively donating transgenic MADM-7 and Talin1floxed mice, and Ekaterina
894 Papusheva for providing a custom 3D channel alignment script. This work was supported by
895 European Research Council grant ERC-CoG-72437.
896

Contributions

897 F.P.A. designed experiments, and performed all *in vivo* and *ex vivo* experiments with
898 assistance of M.H., M.B., S.S and G.K.; J.A. cleared samples and did light-sheet imaging,
899 F.P.A. did all other fluorescent imaging. W.A.K. processed samples for electron tomography,
900 and W.A.K., T.C. and F.P.A. acquired tomograms. F.P.A. did all data processing and analysis
901 with help of R.H., S.S. and G.K; R.H. wrote all custom analysis scripts. S.H. and E.H. aided in
902 the interpretation of MADM and mechanical data, respectively. S.L discussed data. M.S.
903 directed the study, F.P.A. and M.S. wrote the manuscript, and all authors critically reviewed
904 the manuscript.

Ethics declarations

The authors declare no competing interests.

905

906 **Figure 1.** The reactive lymph node resists swelling. **(a)** Side-view focus-stack of popliteal LNs
907 in homeostasis (D0) and inflammation (D14). Scale bar = 500 μm . **(b)** Volumes of swelling
908 LNs calculated from 2D-side views over the course of two-week following onset of
909 immunization. Means \pm SEM are connected (blue line) and a linear regression line (dashed)
910 has been fitted to the data. **(c-d)** Overview of the stress-relaxation experiment on explanted
911 popliteal LNs (D2 of inflammation depicted). **(c)** Measured geometrical parameters are
912 annotated on 2D-side images acquired during a measurement. Scale bar = 300 μm . **(d)** The
913 stress relaxation curve is given by the measured force over time from which the equilibrium
914 force (long timescale) parameter), viscosity (medium timescale) and Young's Modulus (short
915 timescale) relaxation parameters are derived. **(e-g)** Quantification of tissue properties in
916 homeostasis (D0) and inflammation (D2, D4, D8, D14) derived from the stress relaxation
917 curve and geometrical properties. Each datapoint represents a single measured LN.
918 Measurements are pooled from LNs harvested from at least 5 mice and multiple
919 experiments. Mean \pm SEM. **(e)** Quantification of the effective resistance. **(f)** Quantification of
920 the viscosity. **(g)** Quantification of the Young's Modulus. For statistical analysis see
921 Supplementary Information, table 1. *P<0.05, **P<0.01, ****P<0.0001.

922

923 **Figure 2.** Lymphocyte numbers generate pressure and drive lymph node swelling. **(a-j)**
924 Analysis of stress-relaxation experiments on explanted LNs. Each datapoint represents a
925 single measured LN. Measurements are pooled from LNs harvested from at least 5 mice and
926 multiple experiments. Mean \pm SEM are given. **(a)** Side-view of explanted homeostatic LNs
927 from mice treated with anti-CD62L or PBS. Scale bars = 300 μm . Dashed lines depict the
928 outline of LNs. **(b)** Quantification of LN volume. **(c)** Quantification of the effective resistance.
929 **(d)** Quantification of the viscosity. **(e)** Quantification of the Young's Modulus. **(f)** Side-view of
930 explanted D4 inflamed LNs from wt and OTII mice treated with anti-CD62L or PBS. Scale bars
931 = 400 μm . Dashed lines depict the outline of LNs. **(g)** Quantification of LN volumes. **(h)**
932 Quantification of the effective resistance. **(i)** Quantification of the tissue viscosity. **(j)**
933 Quantification of the Young's Modulus. For statistical analysis see Supplementary
934 Information, table 1. ns, not significant. *P<0.05, **P<0.01, ***P<0.001,
935 ****P<0.0001.

936

937 **Figure 3.** The FRC network stretches upon lymph node swelling. **(a)** Overview of the FRC
938 network gap analysis. Left: mGFP labeled FRCs (green), middle: segmented FRC network
939 (white), right: gaps (randomly colored circles) in the FRC network. Scale bar = 20 μ m. **(b)**
940 Representative images of FRC networks gaps in homeostasis (D0) and inflammation (D2, D4,
941 D8 and D14). **(c)** Averaged and smoothed distribution of FRC network fitted circle
942 distribution plotted as the Weighted Area Fraction as a function of the fitted circle diameter.
943 **(d)** Quantification of the mean fitted-circle diameter. Each datapoint represents the average
944 value of 10-30 analyzed consecutive sections of an acquired 3D volume. Means for each
945 timepoint are depicted as a black line. Data are for each timepoint pooled from 5 popliteal
946 or inguinal LNs from at least 3 mice and 2 separate experiments. For statistical analysis see
947 Supplementary Information, table 1. ***P<0.001, ****P<0.0001.

948

949 **Figure 4.** Conduits are stretched in the swelling lymph node. **(a)** Overview of STEM
950 tomography acquisition of macerated LN samples. Images show the fibrillar collagen of T
951 zone conduits at a single tilt angle, and a maximum intensity projection crop of a 3D conduit
952 reconstructed from multiple tilting angles. **(b)** Representative 3D reconstructions of fibrillar
953 collagen (blue) from macerated conduits at homeostasis (day 0) and inflammation (D2, D4
954 and D14) in which the conduit center line (yellow) and tracked fibril segments (grey) are
955 annotated. **(c)** Visual representation of the conduit fibril alignment analysis of an imaged 3D
956 conduit volume. Angles of individual fibril segments (thick colored lines) with the center line
957 of the conduit (dashed black line) are measured at multiple points along the fibril segment
958 (thin colored lines) and averaged per fibril segment. **(d)** Quantification of conduit fibril
959 alignment with center line. Each datapoint represents an individual fibril segment. Means
960 are depicted as black lines. For statistical analysis see Supplementary Information, table 1.
961 ns, not significant. ***P<0.001, ****P<0.0001.

962

963 **Figure 5.** FRC network tension increases upon lymph node swelling. **(a)** Overview of *in vivo*
964 UV-laser cut experiment of the FRC network. Inguinal LNs from FRC-mGFP mice are
965 surgically exposed and kept hydrated at 37°C. A high UV-laser cuts the FRC network along 10
966 μ m at 3 different planes after which the local recoil of the FRC network is imaged. Scissor
967 and line indicate cutting location and arrows the recoiling FRC network. Scale bars = 20 μ m.
968 **(b)** Representative example of FRC network recoil. Images depict stills from before (t=-1s),

969 directly after ($t=0s$) and late after ($t=6.2s$) cutting (scale bars = 5 μm), with corresponding
970 kymograph along the recoil axis (scale bar x-axis = 1s, y-axis = 2 μm). Scissor and line
971 indicate cutting location and arrows the recoiling FRC network. Dashed lines in kymograph
972 indicate slopes used to calculate the recoil velocity, and vertical white line the cut. **(c)**
973 Quantification of recoil velocity from kymographs. Each datapoint represents a single FRC
974 network cut. Data is pooled from 3-4 animals and at least 2 experiments per analyzed
975 timepoint. Means \pm SEM are depicted and connected with a line. **(d)** 3D view of the FRC
976 network and stained for YAP/TAZ. Stack size 20 μm . Scale bar = 20 μm . **(e)** Representative
977 examples of YAP/TAZ nuclear and cytoplasmic localization. N:C = nuclear to cytoplasmic
978 fluorescent intensity ratio. **(f)** Quantification of YAP/TAZ N:C ratio. Dashed line indicates an
979 equal ratio. Each datapoint corresponds to a single measured FRC. Measurements are taken
980 from a total of 3 LNs per analyzed timepoint from at least two separate experiments.
981 Means \pm SEM are depicted and connected with a line. For statistical analysis see
982 Supplementary Information, table 1. ns, not significant. * $P<0.05$, ** $P<0.001$, **** $P<0.0001$.
983

984 **Figure 6.** FRCs in the swelling lymph node undergo distributed clonal expansion. **(a)**
985 Schematic overview of the sparse mosaic analysis with double markers (MADM) labeling
986 approach for FRC cluster imaging. **(b-k)** Quantification of light sheet images from cleared
987 LNs in homeostasis (D0) and inflammation (D4 and D8). All graphs depict the mean \pm SD. Each
988 datapoint represents a single popliteal LN. LNs are retrieved from at least 3 mice and 2
989 separate experiments for each condition. **(b)** LN volumes. **(c)** Numbers of MADM labeled
990 FRCs. **(d)** Numbers of FRCs found in clusters. **(e)** Number of clusters. **(f)** 3D view of HEVs
991 (grey) and smoothed convex-hull of cluster volumes (randomly colored) in a homeostatic
992 (D0) and inflamed (D4) LN, scale bar = 200 μm **(g)** Frequency distribution of FRC cluster sizes
993 found in observed and simulated data in homeostasis (D0) and inflammation (D4 and D8).
994 **(h)** Quantification of the cluster factor (CF) between homeostatic (D0) and inflamed LNs (D4
995 and D8). **(i)** Number of FRC clusters in homeostatic (D0) and inflamed LNs (D4 and D8)
996 plotted as a function of the distance from the nearest HEV. **(j)** Correlation-matrix of paired
997 variables assessed in the cluster analysis. Spearman correlation: p -values are given and the
998 correlation-coefficients are color-coded. **(k)** CF plotted as a function of the LN volume. A
999 spline-fit is plotted through the data-points. For statistical analysis see Supplementary
1000 Information, table 1. ns, not significant. ** $P<0.01$, *** $P<0.001$, **** $P<0.0001$.

1001

1002

1003 **Figure 7.** Talin1 is required for FRC mechanosensing. **(a)** Quantification of LN weights in
1004 homeostasis and following inflammation (D4 and D14) in control and FRC^{ΔTalin1} mice. Each
1005 datapoint represents a single LN. Data is pooled from at least 5 mice from multiple
1006 experiments per condition. Insert depicts the grow curves of the plotted data fitted with a
1007 non-linear regression function. Mean±SEM. **(b)** T zone FRC network of FRC-mGFP (control)
1008 and FRC^{ΔTalin1}-GFP mice stained for YAP/TAZ. Enlargements depict representative examples
1009 of the N:C of YAP/TAZ. Scale bars = 10 μm. **(c)** Quantification of YAP/TAZ localization in FRCs
1010 of control and FRC^{ΔTalin1} mice in homeostasis (D0) and at inflammation (D4). Mean±SEM. **(d)**
1011 Representative 3D images of 3D network analysis of control and FRC^{ΔTalin1} mice in
1012 homeostasis (D0) and following inflammation (D4 and D14). Imaged stack size: 100-300 μm.
1013 Scale bars = 50 μm. **(e)** Quantification of FRC network analysis as shown in **d**. Left: average
1014 weighted volume fraction plotted as function of the sphere diameter. Right: average sphere
1015 diameter for all conditions. Each datapoint represents an individual LN from at least 3 mice
1016 and 2 experiments per condition. Means are depicted by black lines. **(f)** Quantification of
1017 cleaved Caspase3+ FRCs from FRC-mGFP (control) and FRC^{ΔTalin1}-GFP mice in homeostasis
1018 (D0) and inflammation (D4 and D8). Each datapoint represents a single LN. Data pooled
1019 from 3 mice per timepoint. Images depict the identification of an apoptotic FRC. Scale bar =
1020 3 μm. **(g)** Quantification of Ki67+ FRCs from FRC-mGFP (control) and FRC^{ΔTalin1}-GFP mice in
1021 homeostasis (D0) and inflammation (D4 and D8). Each datapoint represents a single LN.
1022 Images depict the identification of a proliferating FRC. Scale bar = 3 μm. Data pooled from 3
1023 mice per timepoint. Mean±SD. For statistical analysis see Supplementary Information, table
1024 1. ns, not significant. *P<0.05, **P<0.01, ***P<0.001, ****P<0.0001.

1025

1026 **Figure 8.** Capsule fibrosis constrains lymph nodes at late timepoints. **(a)** Overview of
1027 intravital UV-laser cut experiments of the SCS fLECs. Inguinal LNs from FRC-mGFP mice, in
1028 which SCS fLECs are sparsely labeled with a mGFP are surgically exposed. A high UV-laser
1029 cuts the cell along 20 μm in one plane after which the local recoil is imaged. Images depict
1030 stills from before (t=-1s), directly after (t=0s) and late after (t=10.2s) cutting (scale bars = 5
1031 μm), with corresponding kymograph along the recoil axis (scale bar x-axis = 1s, y-axis = 2
1032 μm). Scissor and line indicate location of cut and arrows the recoiling cell. Dashed lines in

1033 kymograph indicate slopes used to calculate the recoil velocity, and vertical white line the
1034 cut. **(b)** Quantification of experiments as described in **a** for homeostatic (D0) and inflamed
1035 (D2, D4, D8, D14) LNs. Each datapoint represents a recoil-measurement of a single fLEC.
1036 Data pooled from 3 mice and at least two experiments. Mean \pm SEM are depicted and
1037 connected with a line. **(c)** Representative confocal images of LN capsules from PROX1-GFP
1038 mice in homeostasis (D0) and inflammation (D4, D8 and D14), in which LECs are labeled by a
1039 cytoplasmic GFP. Mesenchymal cells are stained for PDGFR- β , and nuclei are counterstained
1040 with DAPI. Scale bars = 20 μ m. **(d)** Quantification of the capsule thickness measured from
1041 the SCS as depicted in **c**. Each datapoint represents the average of 3 measurements per LN.
1042 Mean \pm SEM are connected with a line. Data pooled from 5 LNs derived from 3 mice per
1043 timepoint. **(e)** Overview of micro-pipette assay for capsule stiffness measurements.
1044 Capsules of explanted popliteal LNs are labeled by brief incubation with Alexa Fluor 647-
1045 conjugated anti-ERTR7 antibody, upon which a small diameter glass pipette is placed on the
1046 capsule and a defined negative pressure applied. The ECM 'tongue' entering the pipette is
1047 subsequently measured. The local effective Young's Modulus of the capsule is derived using
1048 Laplace's law. Scale bar = 50 μ m. **(f)** Quantification of measurements as described in **e** for
1049 homeostatic (D0) and inflamed (D2, D4, D8 and D14) LNs. Each datapoint represents the
1050 average of 3 measurements per LN. Mean \pm SEM are connected with a line. Data pooled from
1051 5 LNs derived from 3 mice per timepoint. **(g)** Quantification of the Capsule swelling
1052 resistance as measured by the Passive Tension, given by multiplying the capsule thickness
1053 and Young's modulus from **d** and **f**, respectively. Each datapoint represents a single LN.
1054 Mean \pm SEM are connected with a line. **(h)** Schematic of the mechanical dynamics of the
1055 swelling LN. For statistical analysis see Supplementary Information, table 1. ns, not
1056 significant. **P<0.01, ***P<0.001.

1057 **Supplementary Figure 1.** **(a)** Quantification of popliteal LN volumes calculated from 2D side
1058 views in homeostasis (D0) and inflammation (D2, D4, D8, D14) acquired from parallel plate
1059 compression experiments. Mean \pm SEM. **(b)** Relation between calculated volumes and
1060 measured weights of popliteal LNs in homeostasis and inflammation. A regression line is
1061 fitted. **(c)** Example of a double-exponential force fit (red line) on a stress-relaxation
1062 measurement. Arrow indicates the force at equilibrium (F_{eq}). **(d)** Average of stress-relaxation
1063 curves for all measured conditions. Mean \pm SEM. **(e)** Schematic representation of the

1064 generalized Kelvin model and formulas used to calculate tissue properties from parallel
1065 plate stress-relaxation experiments. Adapted from *Forgacs et al.*. **(f)** SEM image of packed
1066 lymphocytes in the LN paracortex. Scale bar = 2 μm . For statistical analysis see
1067 Supplementary Information, table 1. ** $P < 0.01$, **** $P < 0.0001$.

1068 **Supplementary Figure 2.** **(a)** Schematic of LN processing for STEM tomography of T zone
1069 conduits. **(b)** Example of a macerated conduit imaged by STEM in which the characteristic D-
1070 period of collagen fibrils can be observed. Scale bar = 500 μm . **(c)** Examples of a T zone
1071 conduit at different tilting angles acquired by STEM tomography. **(d)** Schematic of a
1072 computed weight back projection to reconstruct a 3D volume of a conduit from differential
1073 tilting angles.

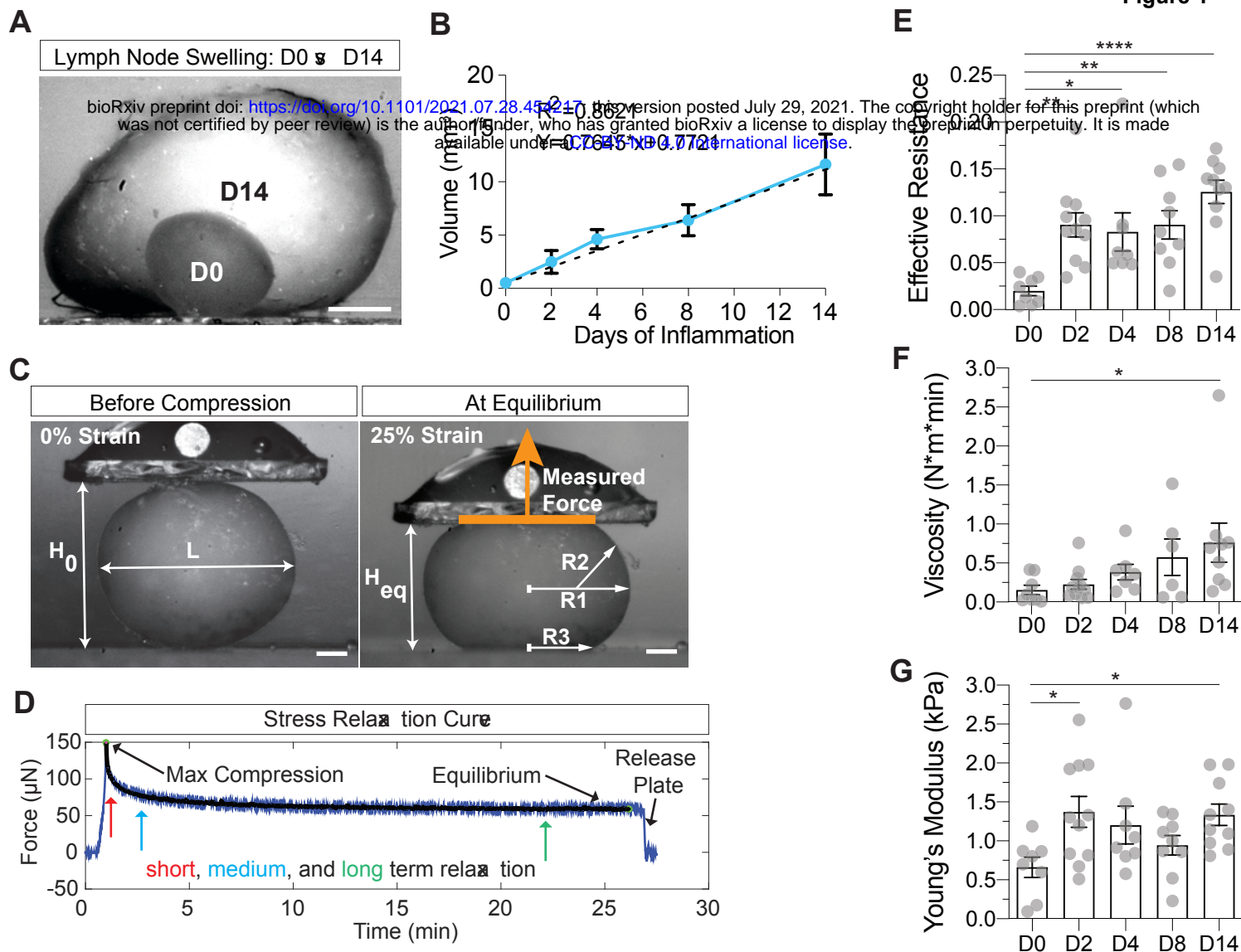
1074 **Supplementary Figure 3.** **(a)** Schematic of the MADM labeling principle. Rare
1075 interchromosomal recombination in the G2 cell cycle phase following x-segregation of
1076 chromosomes labels FRCs with either a cytoplasmic tdTomato or GFP. **(b)** Sparse labeling of
1077 FRCs. Scale bar = 200 μm . **(c)** 3D fluorescent intensity images of GFP labeled FRCs and *in situ*
1078 labeled HEVs by anti-PNAd-ATTO647n antibody. **(d)** Quantification of the MADM labeling
1079 distribution in homeostasis (D0) and inflammation (D4 and D8). Each datapoint represents a
1080 single LN. Mean \pm SD. **(e)** Overview of the labeling of HEVs and mapping of labeled FRCs (only
1081 tdTomato+FRCs are shown) at D4 of inflammation. The enlarged image depicts the mapping
1082 of individual FRCs by a grey sphere at the center of each cell. Scale bars = 200 μm . **(f)**
1083 Formula for the calculation of the cluster factor (CF) per LN. **(g)** Quantification of the
1084 average distance to the nearest neighbor (NN) of both mapped FRCs and randomly localized
1085 FRCs from simulations in homeostasis (D0) and inflammation (D4 and D8). Means are
1086 depicted by black lines. **(h)** Quantification of relative numbers of MADM-labeled FRCs found
1087 in clusters in both homeostasis (D0) and inflammation (D4 and D8). Mean \pm SD. For statistical
1088 analysis see Supplementary Information, table 1. ns, not significant. ** $P < 0.01$, *** $P < 0.001$.

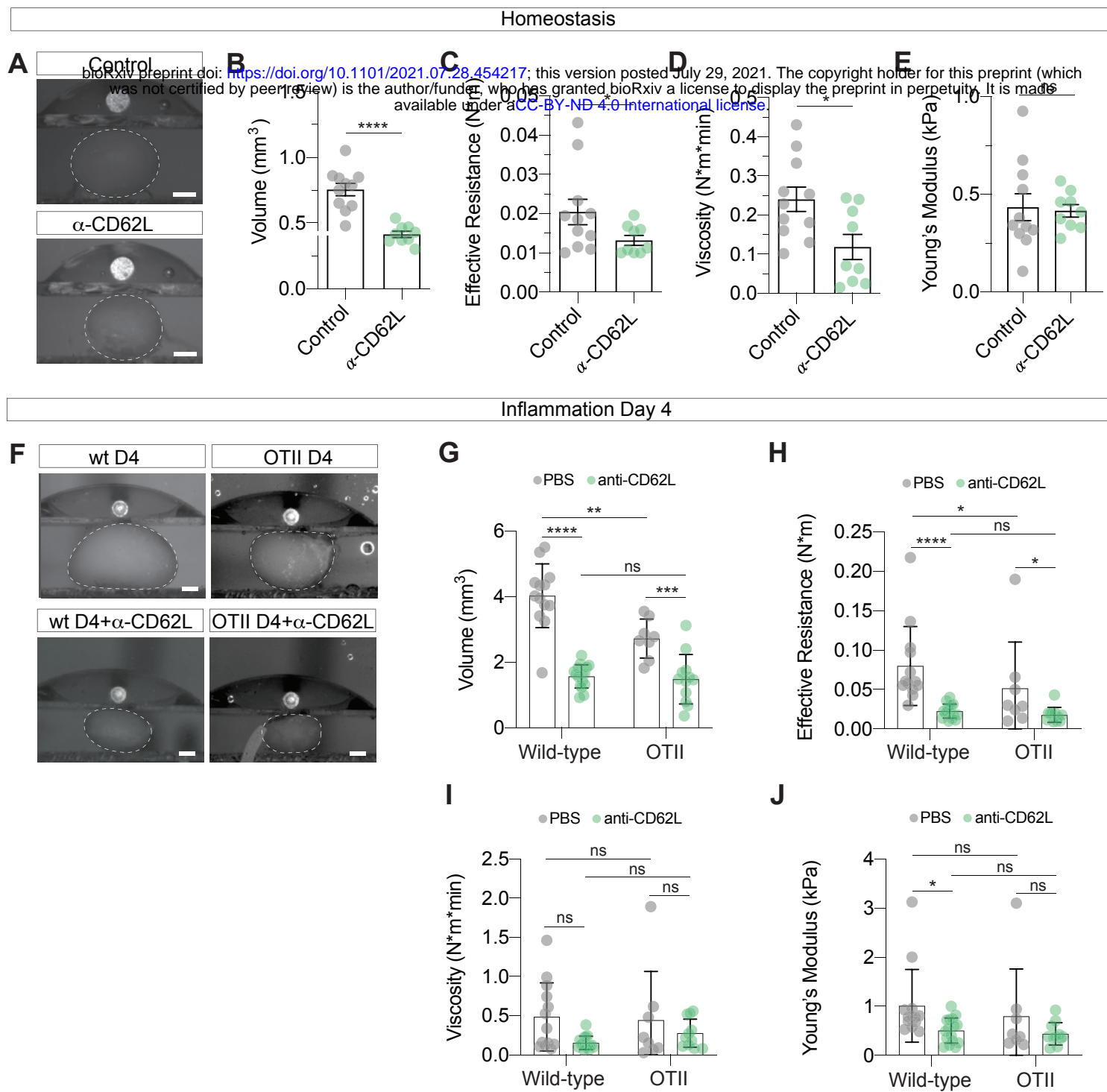
1089 **Supplementary Figure 4.** **(a)** Quantification of steady-state popliteal and inguinal LN weights
1090 from control and FRC ^{Δ Talin1} mice. Each datapoint represents a measured LN. Images show a
1091 representative inguinal LN for each condition. Scale bars = 1 mm. **(b)** Quantification of
1092 steady-state T zone CCL21 protein as measured *in situ* by fluorescent intensity following
1093 staining for CCL21. Measurements are taken from histological sections from 5 LNs of 3 mice

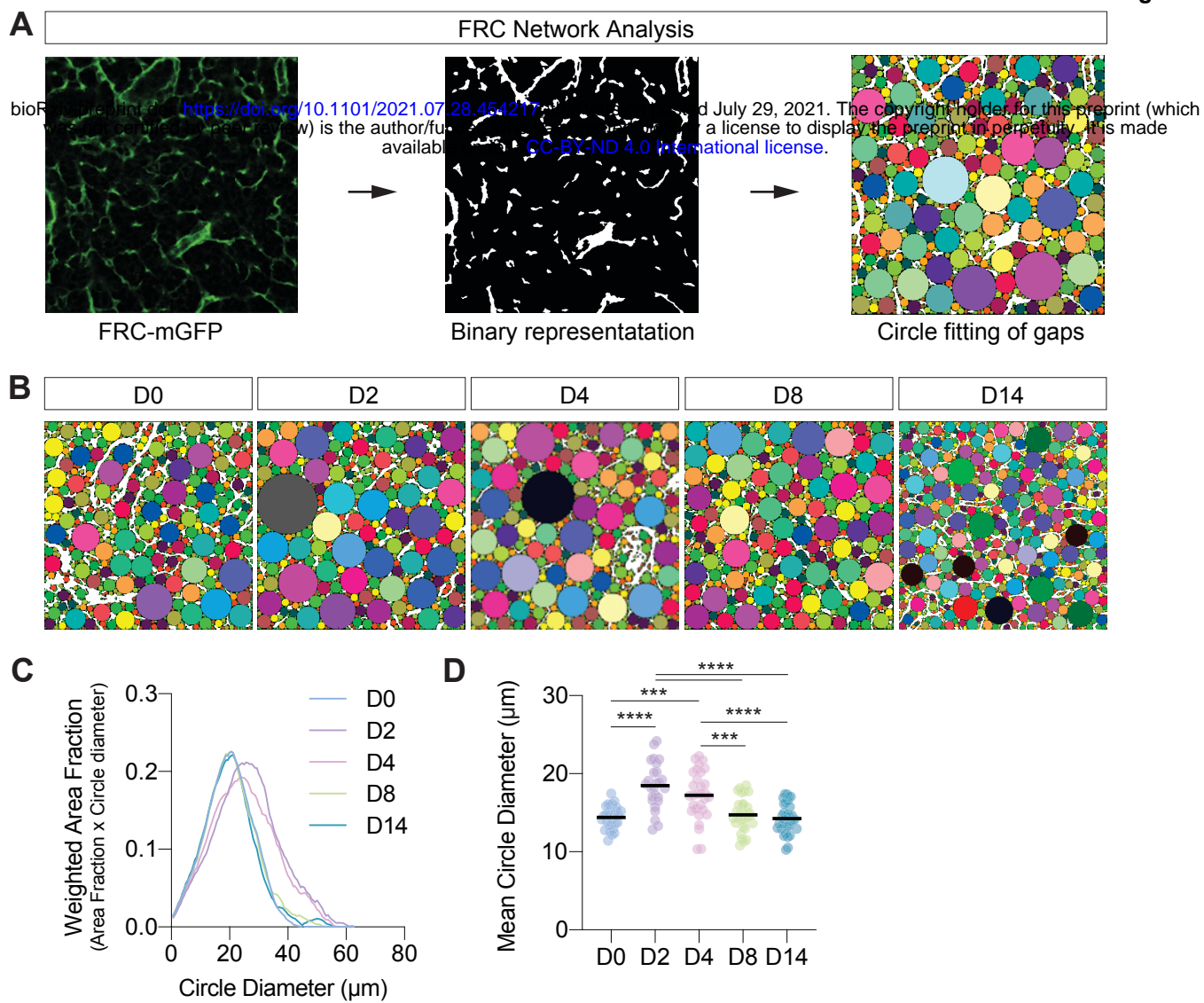
1094 for each condition. Mean±SEM. Scale bars = 20 μm. (c) T zone and B-cell follicles in steady-
1095 state popliteal LNs from control and FRC^{ΔTalin1} mice stained for CD3 (T cells) and B220 (B
1096 cells). Scale bars = 200 μm. (d) ICAM-1, PDPN, VCAM and merged staining from steady-state
1097 popliteal LN T zones from control and FRC^{ΔTalin1} mice. Scale bars = 20 μm. (e) Overview of
1098 the T zone FRC network in homeostasis (D0) and inflammation (D4 and D14) between FRC-
1099 mGFP (control) and FRC^{ΔTalin1}-mGFP mice stained for collagen IV. Scale bar = 50 μm. For
1100 statistical analysis see Supplementary Information, table 1. *P<0.05, ****P<0.0001.

1101 **Supplementary Figure 5.** (a) Ccl19-Cre; mTmG mice sparsely label fLECs of the SCS. Zoomed
1102 window depict the SCS with LECs brightly labeled with tdTomato (mTdT) and the sparsely
1103 labeled fLEC (mGFP), given by the double positive labeling with the fLEC-marker LYVE-1
1104 (gray). (b) Overview of the UV-laser cut experiment on TAMRA labeled capsule ECM of
1105 explanted LNs in homeostasis (D0) and inflammation (D2, D4, D8, D14), which faithfully
1106 represents capsule ECM as observed in alkali macerated LNs imaged by STEM and SEM.
1107 Particle imaging velocimetry (PIV) was used to measure displacement of structures above
1108 and below the cut site from band-pass filtered images. Recoil displacement is depicted by
1109 orange vectors. Scale bar STEM image = 5 μm, SEM image = 1 μm, fluorescent TAMRA-
1110 labeled image = 20 μm. (c) Quantification of recoil velocities of capsule cuts from
1111 experiments on homeostatic (D0) and inflamed (D2, D4, D8, D14) LNs as described in b. Each
1112 datapoint represents a single cut. Between 14 and 24 cuts were taken per measured
1113 timepoint from at least 5 LNs from two animals and at least two separate experiments.
1114 Mean+SEM connected by a line. (d) Representative histological examples of LN capsules
1115 from PROX1-GFP mice in homeostasis and D14 of inflammation, stained for PDGFR-β and
1116 counterstained with DAPI. Scale bars = 200 μm. For statistical analysis see Supplementary
1117 Information, table 1. *P<0.05, **P<0.01.

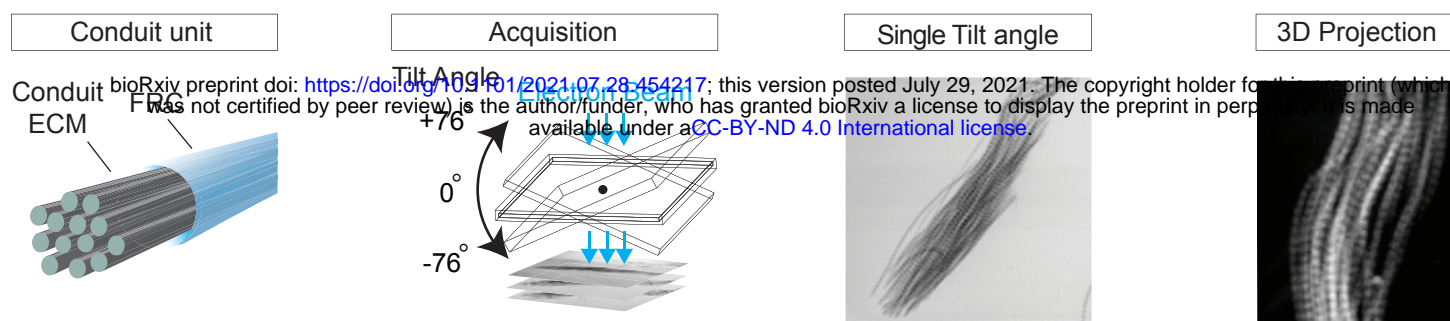
1118 **Supplementary Movie 1.** Example of low (homeostasis; D0) and high tension (Inflammation;
1119 D4) of the FRC network as given by the recoil speed following *in vivo* UV-laser cutting in
1120 surgically exposed inguinal LNs of FRC-mGFP mice.



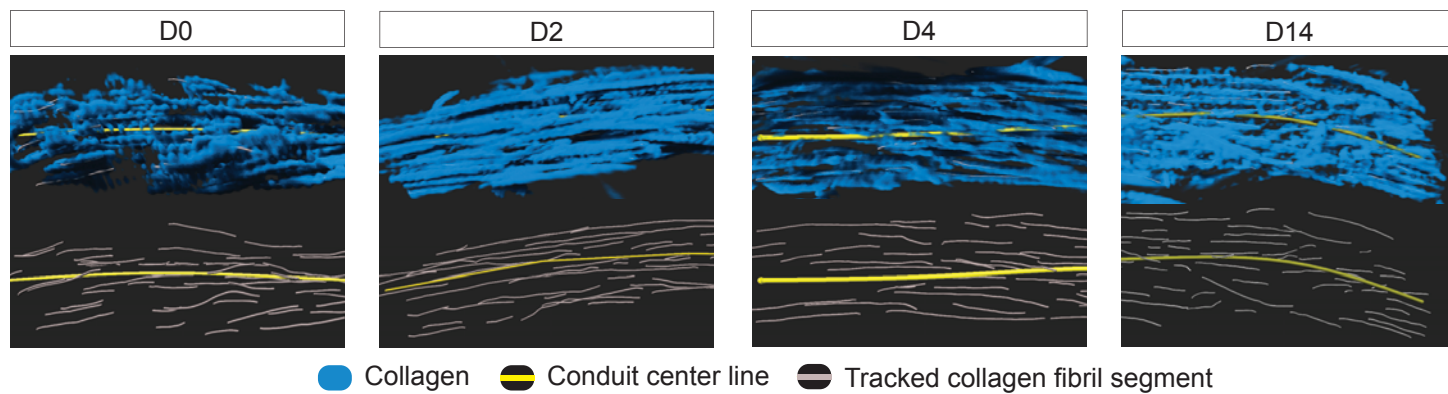




A

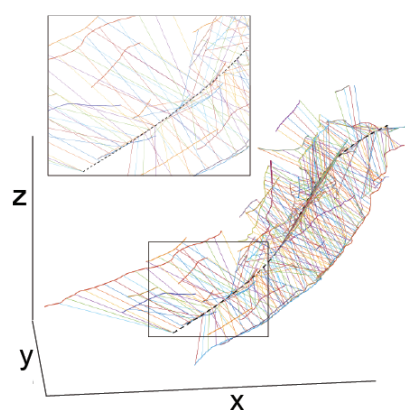


B

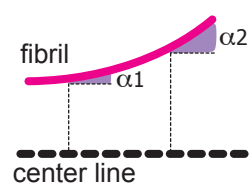


C

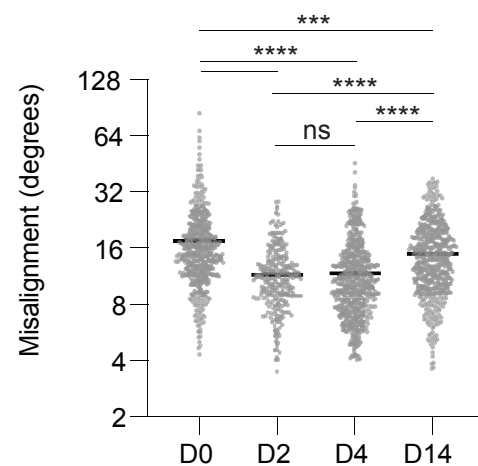
Collagen fibril alignment analysis

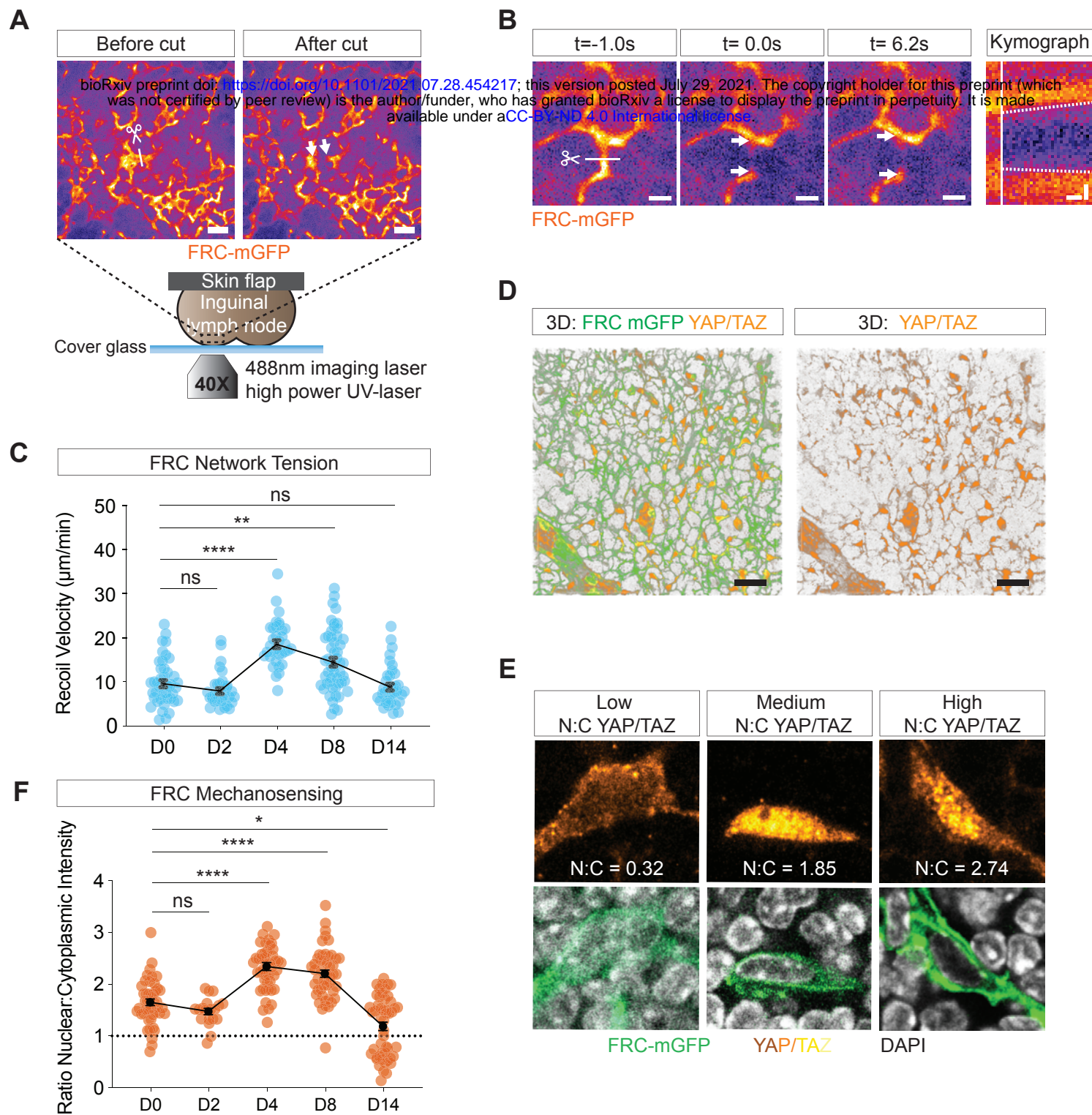


Angle measurements



D





A

Ccl19-Cre hem; MADM-7^{GT/TG}
Sparse MADM labeling of FRCs



Homeostasis Inflammation

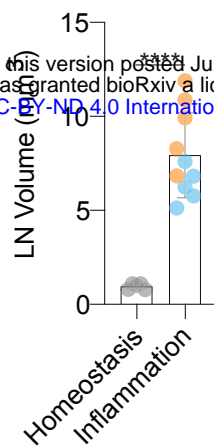
Footpad injection
KLH/CFA

D0 D4 D8

Endpoint analyses

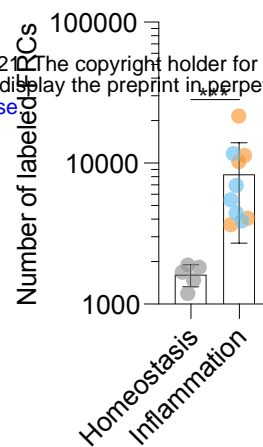
B

●D0 ●D4 ●D8



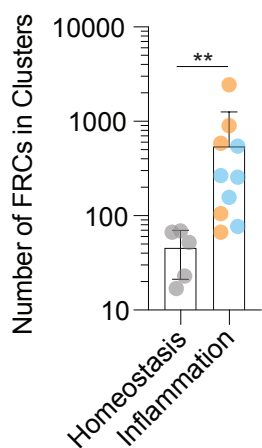
C

●D0 ●D4 ●D8



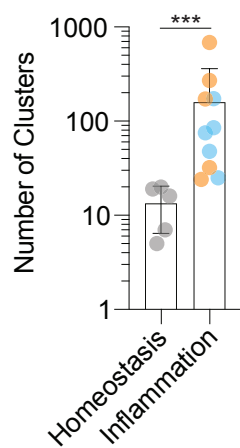
D

●D0 ●D4 ●D8



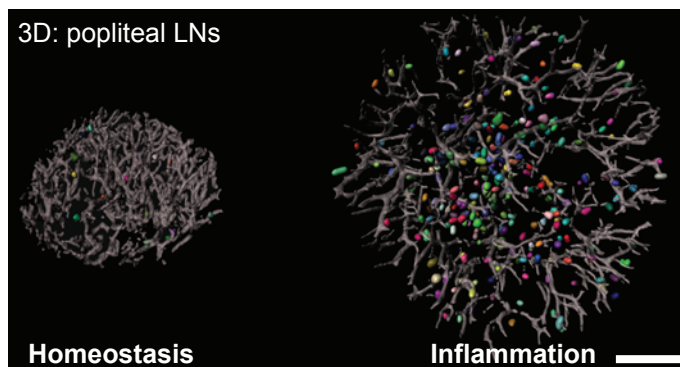
E

●D0 ●D4 ●D8



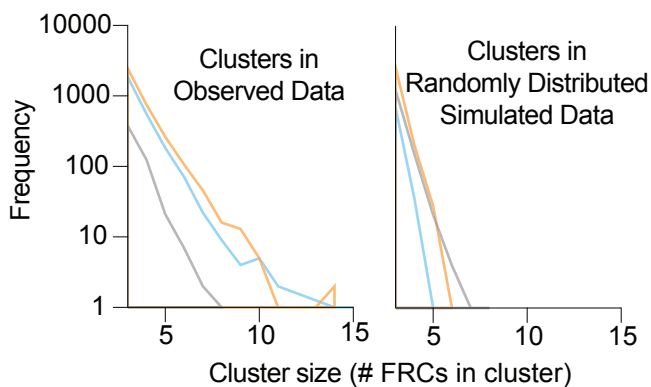
F

FRC Cluster Volumes High Endothelial Venules



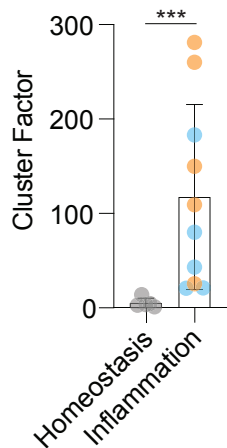
G

●D0 ●D4 ●D8

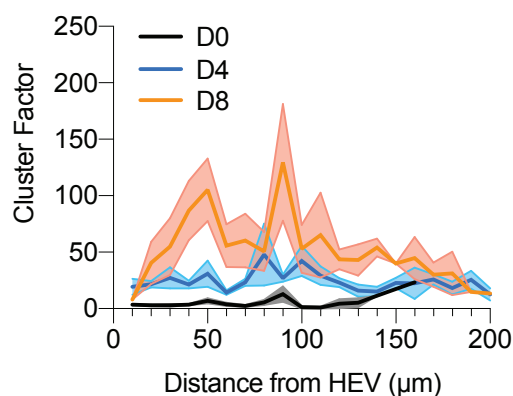


H

●D0 ●D4 ●D8



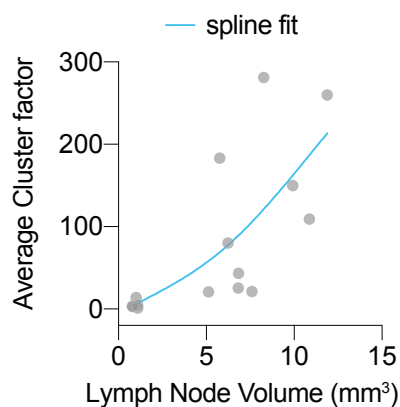
I

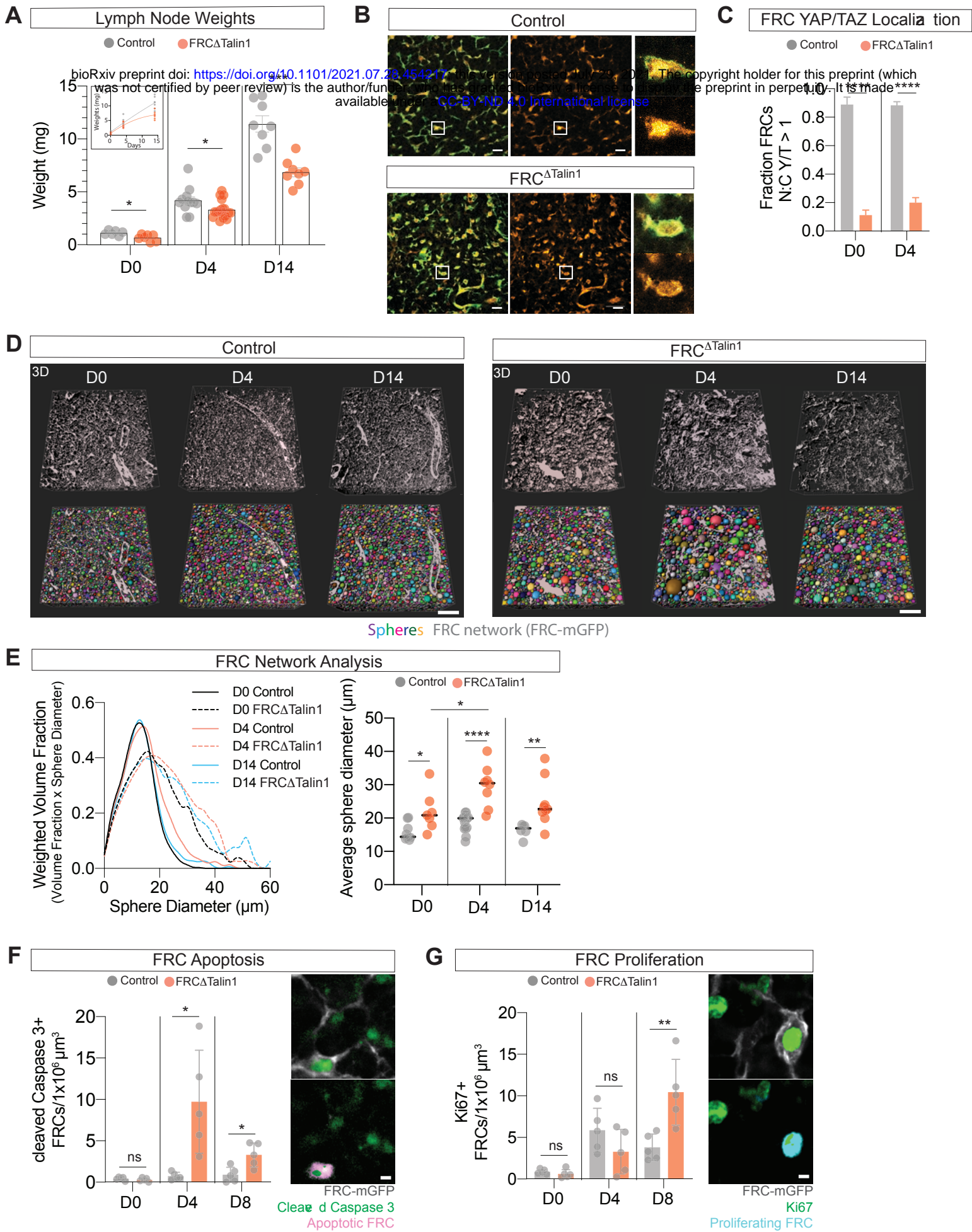


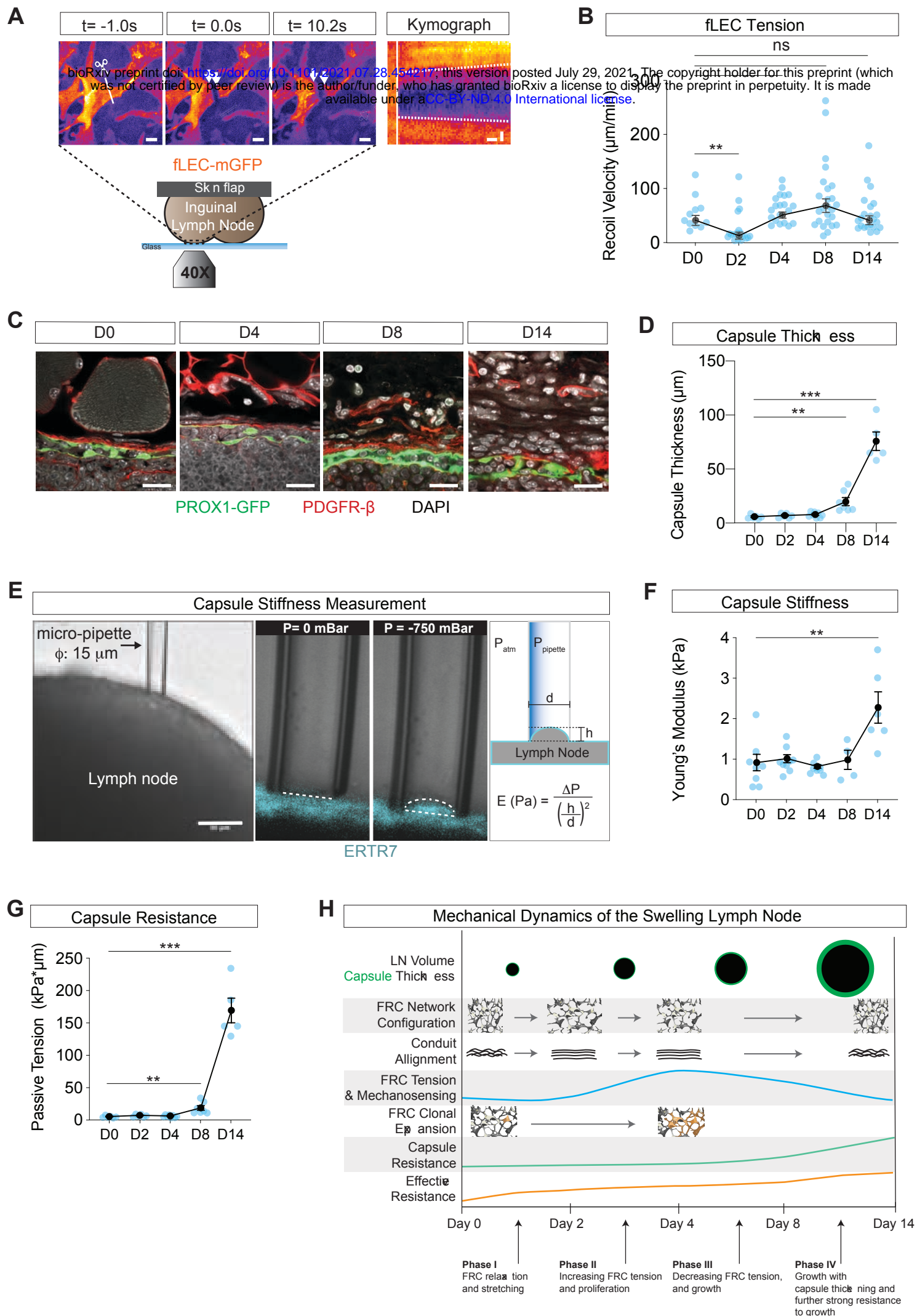
J

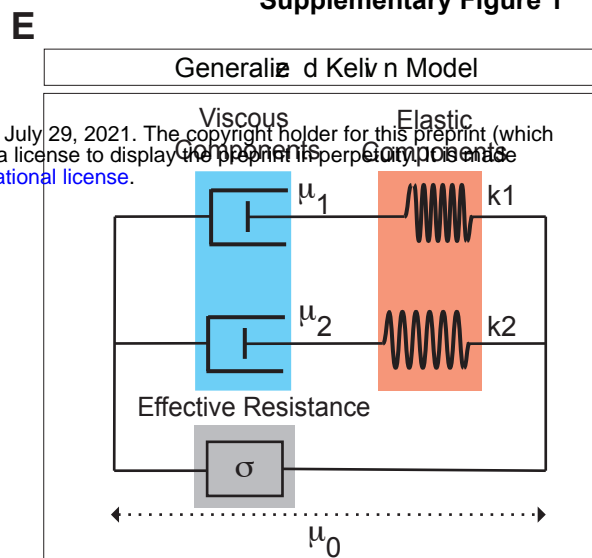
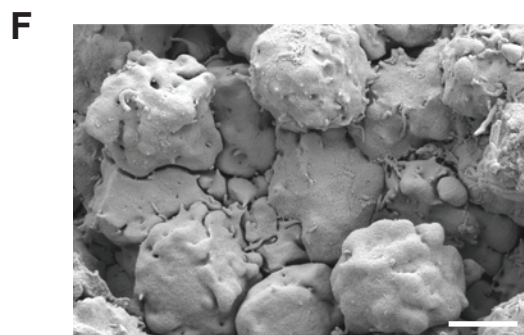
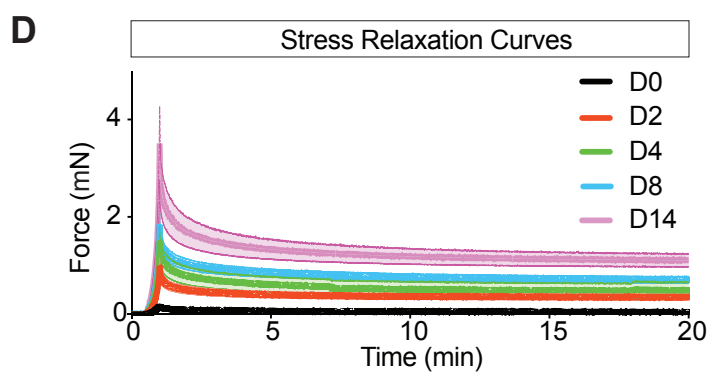
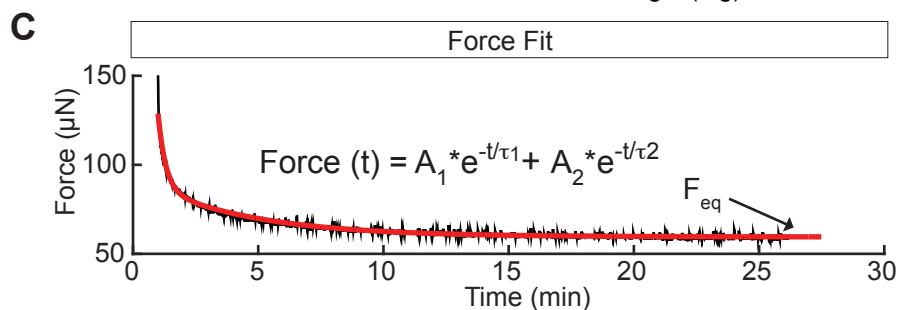
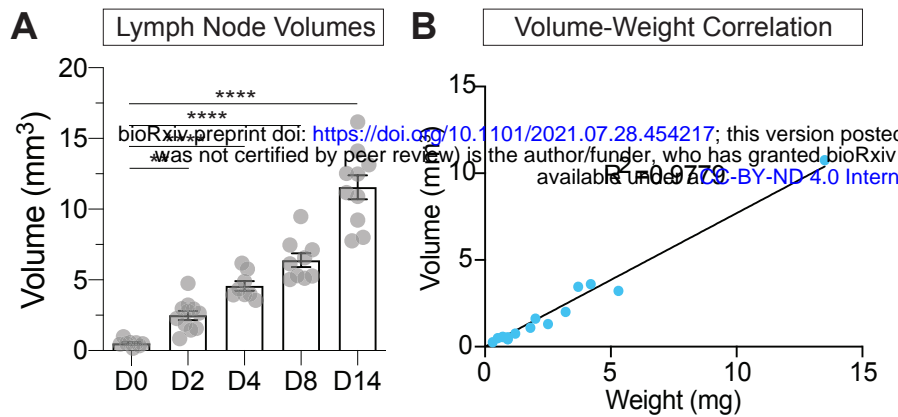
	Cluster Factor	# Labeled FRCs	# Clusters	# FRCs in Clusters	Corr. Coeff.
LN Volume	0.82 ***	0.79 ***	0.70 **	0.68 **	
Cluster Factor		0.58 ns	0.60 ns	0.56 ns	
# Labeled FRCs			0.95 ****	0.93 ****	
# Clusters				0.98 ****	

K

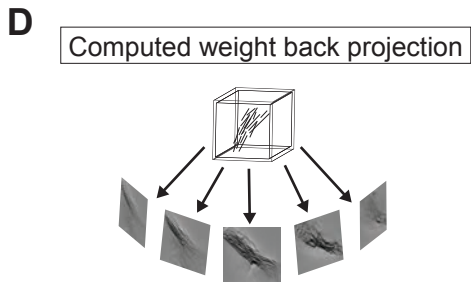
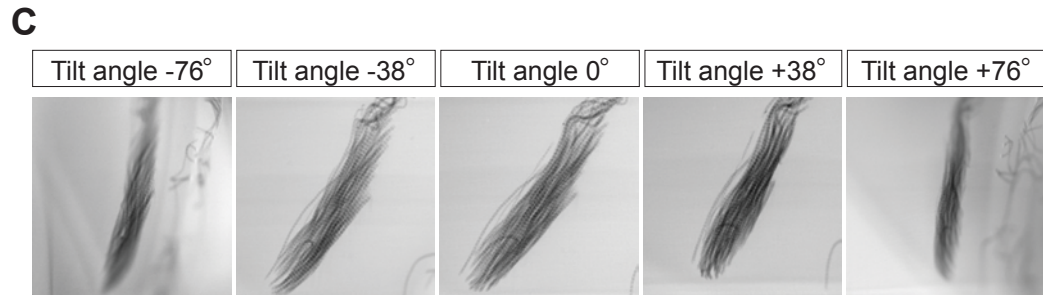
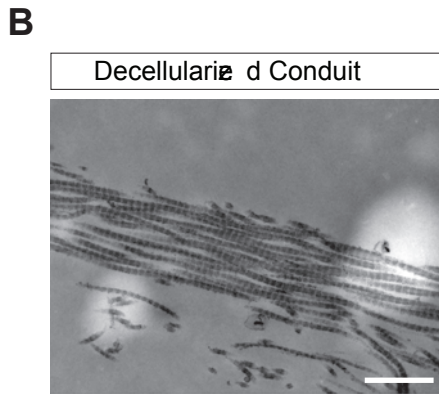
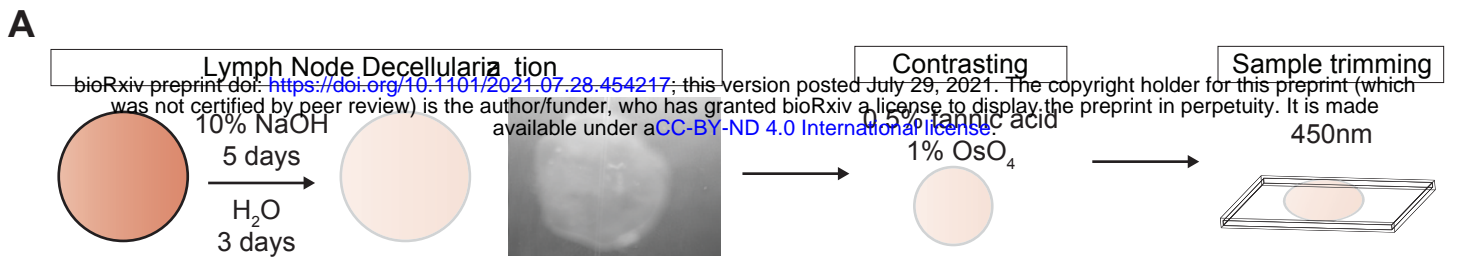








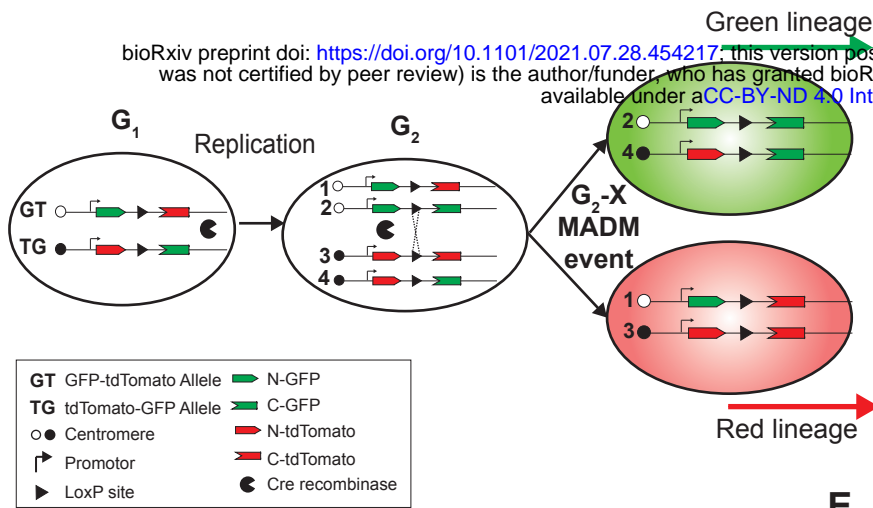
- 1) **Volume** = $(4/3) \pi R^3 (H_0/2)^2$
- 2) **Contact Area** = πR^2
- 3) **Effective Resistance** = σ
is derived from
$$\frac{F_{\text{eq}}}{\pi R^2} = \sigma \left(\frac{1}{R_1} + \frac{1}{R_2} \right)$$
- 4) **Strain** = $1 - (H_{\text{eq}} / H_0)$
- 5) **Stress** = $F_{\text{eq}} / \text{Contact Area}$
- 6) **Elastic Modulus** = $\text{Stress} / \text{Strain}$
- 7) $\mu_0 = F_{\text{eq}} / \sigma$
- 8) $K_1 = A_1 / \mu_0$ $K_2 = A_2 / \mu_0$
- 9) **Viscosity** = $\mu_2 = \tau_2 K_2$



A

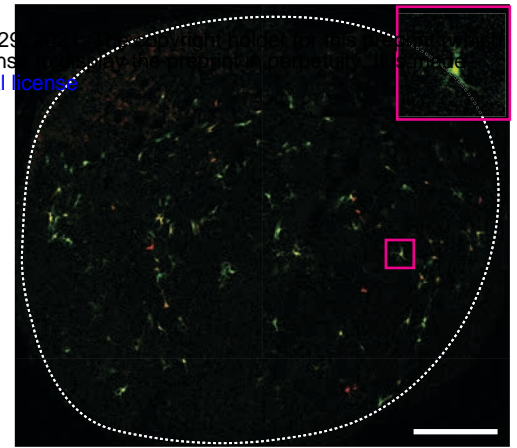
Mosaic Analysis with Double Markers (MADM) Principle

bioRxiv preprint doi: <https://doi.org/10.1101/2021.07.28.454217>; this version posted July 29, 2021. The copyright holder for this preprint (which was not certified by peer review) is the author/funder, who has granted bioRxiv a license to display the preprint in perpetuity. It is made available under aCC-BY-ND 4.0 International license.

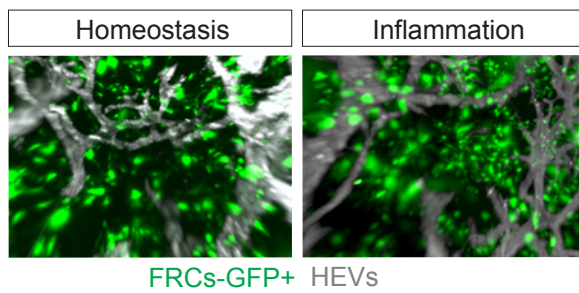


B

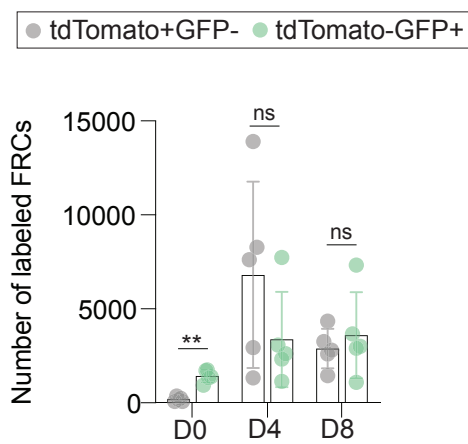
Sparse Labeling of FRCs



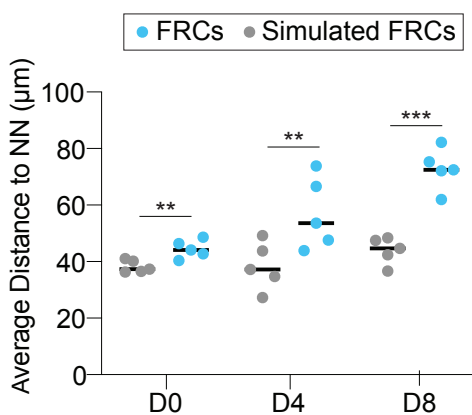
C



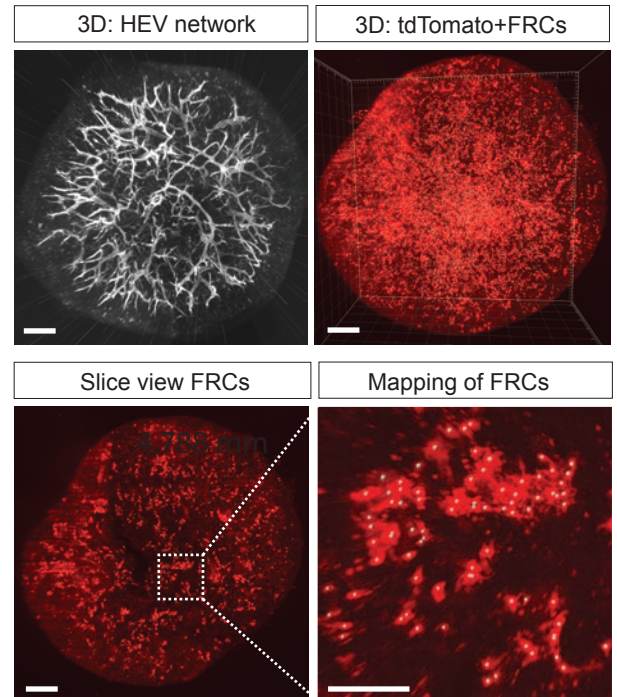
D



G



E



F

Cluster Factor Calculation

$$CF = \frac{\frac{\# \text{ FRCs Clustered}}{\# \text{ FRCs Total}}}{\frac{\# \text{ Simulated FRCs Clustered}}{\# \text{ Simulated FRCs Total}}}$$

H

